Monthly Notices
of the
ROYAL ASTRONOMICAL SOCIETY

MNRAS **474,** 2706–2724 (2018)
Advance Access publication 2017 November 6

doi:10.1093/mnras/stx2835

Orbital tori for non-axisymmetric galaxies

James Binney★

Rudolf Peierls Centre for Theoretical Physics, 1 Keble Road, Oxford OX1 3NP, UK

Accepted 2017 October 30. Received 2017 October 25; in original form 2017 September 7

ABSTRACT

Our Galaxy's bar makes the Galaxy's potential distinctly non-axisymmetric. All orbits are affected by non-axisymmetry, and significant numbers are qualitatively changed by being trapped at a resonance with the bar. Orbital tori are used to compute these effects. Thick-disc orbits are no less likely to be trapped by corotation or a Lindblad resonance than thin-disc orbits. Perturbation theory is used to create non-axisymmetric orbital tori from standard axisymmetric tori, and both trapped and untrapped orbits are recovered to surprising accuracy. Code is added to the `TorusModeller` library that makes it as easy to manipulate non-axisymmetric tori as axisymmetric ones. The augmented `TorusModeller` is used to compute the velocity structure of the solar neighbourhood for bars of different pattern speeds and a simple action-based distribution function. The technique developed here can be applied to any non-axisymmetric potential that is stationary in a rotating from – hence also to classical spiral structure.

Key words: methods: numerical – Galaxy: kinematics and dynamics – galaxies: kinematics and dynamics.

1 INTRODUCTION

From numerically integrated orbits in model gravitational potentials it has long been known that most orbits in a galaxy are quasi-periodic (Binney & Spergel 1982, 1984). One may show that any quasi-periodic orbit is confined to a three-dimensional torus in six-dimensional phase space (Arnold 1989). It is convenient to label each such torus by the Poincaré invariants associated with three closed paths around the torus that cannot be deformed into one another without leaving the torus (e.g. Binney & Tremaine 2008). These labels are known as actions J_i, and they are singled out from other integrals of motion, in particular energy, in that can be complemented by canonically conjugate 'angle' variables θ_i. The latter quantify position within a torus.

Usually orbital tori are nested one inside another, so a non-negligible volume of phase space is filled by such a set of nested tori, and the coordinates $(\boldsymbol{\theta}, \boldsymbol{J})$ constitute an exceedingly convenient set of canonical coordinates for this region. In certain exceptional potentials, a single system of tori completely fills phase space, so there is a global system of action-angle coordinates. Such potentials are said to be 'integrable'. The potentials studied by Stäckel and named after him (e.g. Binney & Tremaine 2008), which yield separable Hamilton–Jacobi equations, are the best known and most important integrable potentials.

By Jeans' theorem (Jeans 1915), the distribution function (DF) f of a steady-state galaxy can be assumed to be a function of whatever isolating integrals are admitted by the galaxy's potential. Hence, wherever in phase space orbits are quasi-periodic, we may take the DF to be a function $f(\boldsymbol{J})$ of the action integrals, and there are cogent reasons (e.g. Binney & McMillan 2016) why it is advantageous to assume that f depends only on $\boldsymbol{J}$ rather than directly on the Hamiltonian $H(\boldsymbol{J})$, as has normally been assumed in the past. If the galactic potential is integrable, the DF can be a single function of $\boldsymbol{J}$, while if phase space breaks up into two or more regions, each with its own sequence of nested tori, each region will require its own functional form, and the global DF will be made up of a patchwork of functions $f(\boldsymbol{J})$, each with its own domain of validity.

In a fairly realistic Galactic potential, the orbits of some halo stars near the Sun lie on tori that do not belong to the family that in an integrable potential fills all phase space (Binney & McMillan 2016; Binney 2016, hereafter B16). B16 showed that a remarkably precise quantitative understanding of the orbits of these stars can be achieved through the concept of resonant trapping. Specifically, one uses the torus-mapping technique (Binney & McMillan 2016) to construct an integrable Hamiltonian that rather closely approximates the true Hamiltonian, and then one uses first-order perturbation theory to compute the libration of orbits around resonant orbits in the integrable Hamiltonian.

The trapping discussed by B16 involved the 1:1 resonance between the radial and vertical oscillations of stars. An observational signature of such resonant trapping has yet to be detected, but since the work of Dehnen (1998), who used Hipparcos data to map velocity space for stars near the Sun, it has been known that there are features in this space that are inconsistent with the hypothesis that the DF has the form $f(\boldsymbol{J})$ with $\boldsymbol{J}$ the actions of an integrable axisymmetric potential.

It has long been suspected that non-axisymmetric components of the Galactic potential are responsible for the differences between observations and the predictions of models that assume

★ E-mail: binney@thphys.ox.ac.uk

axisymmetry (De Simone, Wu & Tremaine 2004; Sellwood 2010; Antoja et al. 2011; Hahn, Sellwood & Pryor 2011; McMillan 2013; Pérez-Villegas et al. 2017). Indeed, the Galaxy is known to have a bar, that may extend as far out as $r \sim 5$ kpc (Blitz & Spergel 1991; Binney et al. 1991; Sormani, Binney & Magorrian 2015; Wegg, Gerhard & Portail 2015), and the disc is known to carry spiral structure (e.g. Lépine et al. 2011). Consequently, the assumption of axisymmetry, which has been used with considerable success in a large number of papers (Binney 2012b; Bovy & Rix 2013; Piffl et al. 2014; Binney & Piffl 2015) cannot be more than a starting point for a more sophisticated treatment that includes the bar and spiral structure.

The goal of this paper is to lay the foundations for such modelling by adapting the perturbative approach of B16 to non-axisymmetric potentials. Specifically, a simple model of the Galactic bar is used to trap the tori of a realistic Galactic potential around the corotation resonance (CR) and outer Lindblad resonance (OLR). Perturbation theory yields an analytic model of the trapped tori, so we have for these trapped tori all the functionality of tori constructed for an axisymmetric potential by torus mapping (Binney & McMillan 2016).

The paper is organized as follows. In Section 2, we introduce the model of the potential of a barred Galaxy that we employ subsequently. In Section 3, we explain how the Hamiltonian for motion in a steadily rotating barred potential is decomposed into a part $H_0(\boldsymbol{J})$ that depends only on the actions and a perturbation $H_1(\boldsymbol{\theta}, \boldsymbol{J})$. In Section 4, we present the relevant Hamiltonian perturbation theory. In Section 5, we apply this theory to our model Galaxy, starting in Section 5.1 with the OLR, proceeding in Section 5.2 to the corotation resonance, and concluding with a very brief description of the ILR in Section 5.3. In Section 6, we use these results to examine velocity space at a solar-like location within our model Galaxy. In Section 7, we relate our results to previous work and consider how our results help us to understand the dynamics of a non-axisymmetric disc. In Section 8, we sum up and consider directions for future work.

Appendix A describes enhancements to the publically available code Torus Mapper (TM), which enable one to construct and manipulate non-axisymmetric orbital tori, whether resonantly trapped or circulating. TM can be can be downloaded from https://github.com/PaulMcMillan-Astro/Torus. Appendix B provides the theoretical structure that TM uses to find the velocities at which a trapped torus passes through a given point.

We use throughout Galactocentric polar coordinates (R, z, ϕ) with the long axis of the bar along $\phi = 0$. Quantities referring to the azimuthal angle ϕ are always listed last because in an axisymmetric potential motion in ϕ is slaved by angular-momentum conservation to the autonomous and sometimes complex motion in the Rz plane.

2 THE GALACTIC POTENTIAL

We frame our discussion in the context of a gravitational potential that McMillan (2011) fitted to a variety of data for our Galaxy. Specifically, we adopt the 'best' potential in that paper, which is generated by thin and thick stellar discs, a flattened (axisymmetric) bulge and a spherically symmetric dark halo. Its local circular speed is $v_c = 239\,\mathrm{km\,s^{-1}}$. Our discussion would not differ materially, however, had we adopted any reasonably realistic axisymmetric potential. To evaluate the potential and its derivatives, we use the FALPOT code distributed in the TM package, which implements an algorithm described by Dehnen & Binney (1998), and was extracted from Walter Dehnen's FALCON package (https://github.com/Milkyway-at-home/nemo/tree/master/nemo_cvs/usr/dehnen/falcON).

2.1 Non-axisymmetric component

We add to the axisymmetric potential a non-axisymmetric perturbation, so

$$\Phi(R, z, \phi) = \Phi_0(R, z) - \Phi_2(R, z)\cos 2\phi. \tag{1}$$

The non-axisymmetric contribution to the density is

$$\begin{aligned}\rho_2(R, z, \phi) &= -(4\pi G)^{-1}\nabla^2(\Phi_2 \cos 2\phi)\\ &= -(4\pi G)^{-1}\left(\nabla^2\Phi_2 - 4\Phi_2/R^2\right)\cos 2\phi.\end{aligned} \tag{2}$$

This should vanish at both small and large radii. In fact, as the z-axis is approached, it must vanish at least as fast as R^2. At large R, it should tend to the external potential of a quadrupole, so decay like r^{-3}. These conditions are satisfied by the ansatz

$$\Phi_2(R, z) = \frac{K R^2}{(R_\mathrm{b}^2 + m^2)^{5/2}}, \tag{3}$$

where R_b is a scale radius,

$$m^2 \equiv R^2 + \frac{z^2}{q^2}, \tag{4}$$

and the constant q controls the flatness of the non-axisymmetric contribution to the density. The normalizing constant K in equation (3) has dimensions of velocity squared times length cubed, so it is convenient to control its value through the dimensionless number

$$A \equiv \frac{K}{v_\mathrm{c}^2 R_\mathrm{b}^3}, \tag{5}$$

where v_c is the circular speed at the solar radius that is implied by the axisymmetric component of the potential.

We now have

$$\frac{\mathrm{d}\Phi_2}{\mathrm{d}R} = K R \frac{2R_\mathrm{b}^2 - 3R^2 + 2z^2/q^2}{(R_\mathrm{b}^2 + m^2)^{7/2}}, \tag{6}$$

so

$$\begin{aligned}\frac{1}{R}\frac{\mathrm{d}}{\mathrm{d}R}\left(R\frac{\mathrm{d}\Phi_2}{\mathrm{d}R}\right) = K\big[2\left(2R_\mathrm{b}^2 - 6R^2 + 2z^2/q^2\right)\left(R_\mathrm{b}^2 + m^2\right)\\ - 7R^2(2R_\mathrm{b}^2 - 3R^2 + 2z^2/q^2)\big] \Big/ \left(R_\mathrm{b}^2 + m^2\right)^{9/2}.\end{aligned} \tag{7}$$

Similarly

$$\frac{\mathrm{d}\Phi_2}{\mathrm{d}z} = -5K\frac{R^2}{q^2}\frac{z}{(R_\mathrm{b}^2 + m^2)^{7/2}}, \tag{8}$$

and

$$\frac{\mathrm{d}^2\Phi_2}{\mathrm{d}z^2} = 5K\frac{R^2}{q^2}\frac{7z^2/q^2 - (R_\mathrm{b}^2 + m^2)}{(R_\mathrm{b}^2 + m^2)^{9/2}}. \tag{9}$$

From these formulae, the density $\rho_2(R, z)$ is readily computed.

2.2 Normalization of the bar

Sormani et al. (2015) simulated the flow in two dimensions of isothermal gas del flow in model Galactic potentials and by comparing the simulations to radio-frequency observations of Galactic gas estimated the pattern speed and amplitude of the bar. They concluded that the bar has to generate a substantial quadrupole moment. We fix the strength of our bar by reference to that of their most successful models.

Whereas we have chosen to work from a simple analytic function for the coefficient of proportionality, $\Phi_2(R, z)$, Sormani et al. (2015) assumed a particular form for the corresponding density:

$$4\pi G\rho_2(\boldsymbol{x}) = A_\mathrm{S}\left(\frac{v_0 \mathrm{e}}{r_q}\right)^2 \mathrm{e}^{-2r/r_q}\sin^2\theta\cos 2\phi, \tag{10}$$

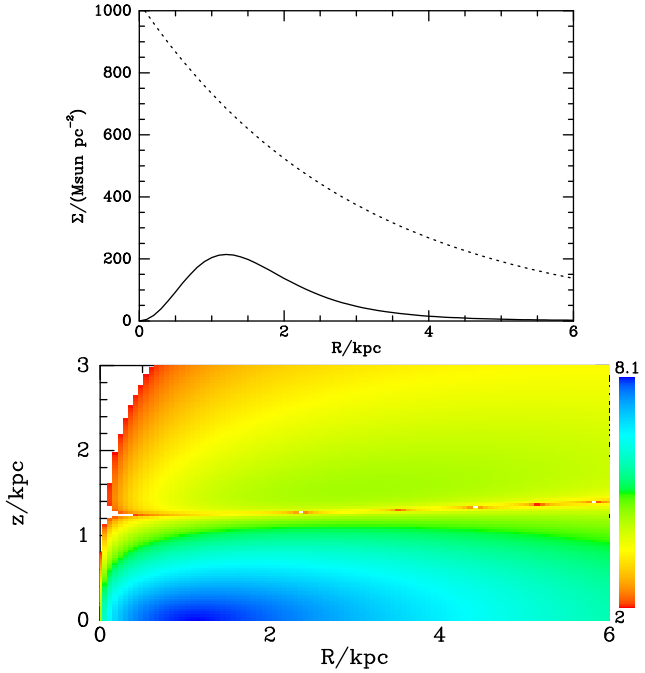

Figure 1. Top: the full curve shows the surface density $\Sigma(R) = \int \mathrm{d}z\, \rho_2(R, z)$ that generates the non-axisymmetric component of the potential (3) with $q = 0.9$, while the dotted curve shows the axisymmetric density to which this is added. Bottom: the density $\rho_2(R, z)$ for the same value of q. The colours indicate values of $\log_{10}\rho_2$. Above the line of three red dots the density is negative.

where $v_0 = 220\,\mathrm{km\,s^{-1}}$, $r_q = 1.5\,\mathrm{kpc}$ and $A_\mathrm{S} \gtrsim 0.4$ is a dimensionless amplitude.

The strength of a bar is quantified by $\lim_{r\to\infty} r^3\Phi_2(\boldsymbol{r})$. Since $\sin^2\theta\cos 2\phi = \sqrt{8\pi/15}\,(Y_2^2 + Y_2^{-2})$, in the notation of equation (2.95) in Binney & Tremaine (2008) at large $\boldsymbol{r}$

$$4\pi G\rho_{22} = A_\mathrm{S}\sqrt{\frac{8\pi}{15}}\left(\frac{v_0\mathrm{e}}{r_q}\right)^2 \mathrm{e}^{-2r/r_q}. \tag{11}$$

Consequently, at large r the potential generated by equation (10) is

$$\Phi_2(\boldsymbol{x}) = A_\mathrm{S}\sqrt{\frac{8\pi}{15}}\frac{Y_2^2 + Y_2^{-2}}{5r^3}\left(\frac{v_0\mathrm{e}}{r_q}\right)^2 \int_0^r \mathrm{d}a\, a^4\mathrm{e}^{-2a/r_q}. \tag{12}$$

For $r \gg r_q$ the integral tends to $4!(r_q/2)^5$, so

$$\begin{aligned} r^3\Phi_2(\boldsymbol{x}) &= \frac{4!\mathrm{e}^2A_\mathrm{S}}{5\times 32}\sqrt{\frac{8\pi}{15}}\,(Y_2^2 + Y_2^{-2})v_0^2r_q^3 \\ &= \frac{3\mathrm{e}^2A_\mathrm{S}}{20}v_0^2r_q^3\sin^2\theta\cos 2\phi. \end{aligned} \tag{13}$$

When $z = 0$ so $m = R = r$, our expression (3) for Φ_2 yields $r^3\Phi_2(r, 0) \to K = Av_\mathrm{c}^2R_\mathrm{b}^3$, so to achieve the same quadrupole as Sormani et al. (2015) we must set

$$A = \frac{3\mathrm{e}^2}{20}\left(\frac{v_0}{v_\mathrm{c}}\right)^2\left(\frac{r_q}{R_\mathrm{b}}\right)^3 A_\mathrm{S}. \tag{14}$$

In this formula, we adopt $v_\mathrm{c} = 239\,\mathrm{km\,s^{-1}}$ and $A_\mathrm{S} = 0.4$.

It remains to choose the bar's scalelength, R_b. Guided by plots like those of Figs 1 and 2, we adopt $R_\mathrm{b} = 2.09\,\mathrm{kpc}$, which is 0.7 times the density weighted disc scalelengths of the axisymmetric component. Then the figures show that the surface density is strongly barred inside $R = 3\,\mathrm{kpc}$ and significantly non-axisymmetric out to $R = 4\,\mathrm{kpc}$. Vertically the bar extends to $|z| \sim 1\,\mathrm{kpc}$.

2.3 Pattern speed

Sormani et al. (2015) concluded that the bar's pattern speed is $\omega_\mathrm{p} \simeq 40\,\mathrm{km\,s^{-1}\,kpc^{-1}}$, a value that coincides nicely the estimate obtained by Wegg et al. (2015) by modelling the kinematics of bulge stars. Pérez-Villegas et al. (2017) show that $\omega_\mathrm{p} = 39\,\mathrm{km\,s^{-1}}$ correctly predicts the kinematics of solar-neighbourhood stars because it causes stars trapped by corotation to visit the solar neighbourhood in the form of the 'Hercules stream'. Over the previous two decades, larger values $\sim$55 $\mathrm{km\,s^{-1}\,kpc^{-1}}$ were favoured, in part on account of a significant underestimate of the length of the bar by Binney et al. (1991) and in part through the Hercules stream being supposed to arise by trapping at the OLR rather than corotation (Dehnen 1998; Monari et al. 2017). In the following, we adopt $\omega_\mathrm{p} = 0.04\,\mathrm{Myr^{-1}} = 39\,\mathrm{km\,s^{-1}\,kpc^{-1}}$.

We take the pattern speed to be positive, so the bar rotates anticlockwise in the xy plane. We usually consider that our Galaxy rotates clockwise because we imagine viewing it from the Northern hemisphere. To apply the present model to our Galaxy, we must view the latter from Australia. The end of the bar that is nearer to the Sun is rotating away from the Sun. We achieve a similar location for a model Sun by placing it at $\phi = 155$ deg.

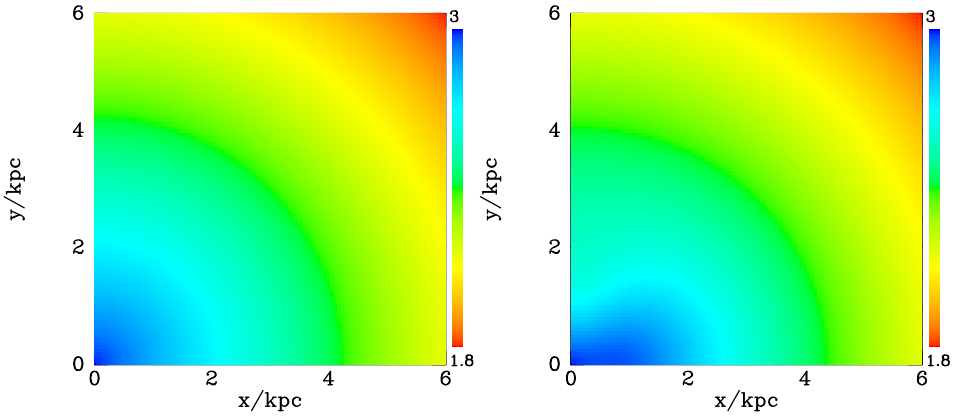

Figure 2. Right: the surface density obtained on adding the non-axisymmetric component plotted in Fig. 1 to the axisymmetric surface density plotted in the left-hand panel. The latter has exponential scalelength $R_\mathrm{d} = 3\,\mathrm{kpc}$.

3 SPLITTING THE HAMILTONIAN

Our goal is to handle perturbations to an axisymmetric system that rotate at a constant angular velocity $\omega_{\rm p}$. Let $\boldsymbol{v}$ be the velocity of a star in the frame of reference that rotates with the system, then the star's kinetic energy is

$$K = \tfrac{1}{2}|\boldsymbol{v} + \omega_{\rm p} \times \boldsymbol{x}|^2, \tag{15}$$

so the Lagrangian is

$$L = \tfrac{1}{2}|\boldsymbol{v} + \omega_{\rm p} \times \boldsymbol{x}|^2 - \Phi(\boldsymbol{x}), \tag{16}$$

where the original time dependence of the gravitational potential Φ has been absorbed into the rotation of the reference frame. It follows from equation (16) that the canonical momentum is

$$\boldsymbol{p} = \frac{\partial L}{\partial \boldsymbol{v}} = \boldsymbol{v} + \omega_{\rm p} \times \boldsymbol{x}, \tag{17}$$

which is in fact the momentum in the underlying inertial frame. The Hamiltonian is

$$H(\boldsymbol{x}, \boldsymbol{p}) = \boldsymbol{p} \cdot \boldsymbol{v} - L = \tfrac{1}{2}|\boldsymbol{p}|^2 + \Phi - \omega_{\rm p} \cdot (\boldsymbol{x} \times \boldsymbol{p}). \tag{18}$$

Since $\boldsymbol{p}$ is the inertial-frame momentum, the first two terms on the right of equation (18) comprise the star's energy in the inertial frame, and the final term is simply $\omega_{\rm p} p_\phi$, where p_ϕ is the component of angular momentum parallel to $\omega_{\rm p}$. Hence, we can write

$$H(\boldsymbol{x}, \boldsymbol{p}) = H_{\rm in}(\boldsymbol{x}, \boldsymbol{p}) - \omega_{\rm p} p_\phi, \tag{19}$$

where $H_{\rm in}$ is the Hamiltonian that would apply if the given potential were not rotating but stationary in an inertial frame. The shift from $H_{\rm in}$ to H that encodes rotation of the potential changes only one equation of motion, namely that of ϕ:

$$\dot{\phi} = [\phi, H] = \frac{\partial H_{\rm in}}{\partial p_\phi} - \omega_{\rm p}. \tag{20}$$

In the rotating frame, ϕ increments more slowly than in the inertial frame because the zero-point of angle is advancing at the rate $\omega_{\rm p}$.

By torus mapping, it will usually be possible to construct a Hamiltonian $\overline{H}(\boldsymbol{J})$ that admits a global system of angle action coordinates $(\boldsymbol{\theta}, \boldsymbol{J})$ and is very close to $H_{\rm in}$. That is, we can write

$$H_{\rm in}(\boldsymbol{\theta}, \boldsymbol{J}) = \overline{H}(\boldsymbol{J}) + H_1(\boldsymbol{\theta}, \boldsymbol{J}), \tag{21}$$

where $H_1 \ll \overline{H}$. If Φ is not very strongly non-axisymmetric, we can map tori in such a way that $\overline{H}$ is axisymmetric, so $p_\phi = J_\phi$ is one of the actions in the set $\boldsymbol{J}$. In this case, the true Hamiltonian

$$H(\boldsymbol{\theta}, \boldsymbol{J}) = \left\{\overline{H}(\boldsymbol{J}) - \omega_{\rm p} J_\phi\right\} + H_1(\boldsymbol{\theta}, \boldsymbol{J}) \tag{22}$$

has been successfully split into a dominant part

$$H_0(\boldsymbol{J}) \equiv \overline{H}(\boldsymbol{J}) - \omega_{\rm p} J_\phi \tag{23}$$

that does not depend on the angle variables and a small perturbation H_1.

It will sometimes be expedient to map tori in such a way that $\overline{H}(\boldsymbol{J})$ is non-axisymmetric. If we do map tori thus, we should be able to arrange for $\overline{H}(\boldsymbol{J})$ to provide a closer approximation to $H_{\rm in}$, and thus make $H_1(\boldsymbol{\theta}, \boldsymbol{J})$ smaller than if we keep $\overline{H}(\boldsymbol{J})$ axisymmetric. The disadvantage of making $\overline{H}$ non-axisymmetric is that then p_ϕ will not coincide with any of the actions in the set $\boldsymbol{J}$ – the way each action depends on $(\boldsymbol{x}, \boldsymbol{v})$ depends on the potential $\Phi(\boldsymbol{x})$, and when Φ is non-axisymmetric, $p_\phi = R^2\dot{\phi}$ will not be an action variable. However, as the degree of non-axisymmetry vanishes, one of the actions, which we may call J_ϕ, will converge on p_ϕ. With a non-axisymmetric $\overline{H}(\boldsymbol{J})$, the $\omega_{\rm p} p_\phi$ term in the full Hamiltonian will contribute to the perturbative part of the Hamiltonian alongside H_1. That is, in this case, we must write

$$H(\boldsymbol{\theta}, \boldsymbol{J}) = \left\{\overline{H}(\boldsymbol{J}) - \omega_{\rm p} J_\phi\right\} + \left[H_1(\boldsymbol{\theta}, \boldsymbol{J}) + (J_\phi - p_\phi)\omega_{\rm p}\right], \tag{24}$$

such that the entire square bracket is a perturbation on the integrable Hamiltonian that is defined by the curly bracket. The residual H_1 from TM will be substantially smaller than the full non-axisymmetric component of the potential with which we will contend, but this gain will be to some extent offset by the appearance of the perturbation $(J_\phi - p_\phi)\omega_{\rm p}$. We leave exploration of this approach to a later study.

4 RESONANCE

Now we present the theory of resonant trapping. This theory relates to the state of *being* trapped by a resonance and does not address the complex process by which a star *becomes* trapped, for example as a bar strengthens and slows down, with the consequence that it sweeps into its embrace stars that previously orbited freely outside it. There is significant overlap between this section and Section 5 of B16, but there are some subtle differences and we need to establish notation for subsequent use.

4.1 Pendulum dynamics

A resonant orbit in $H_0(\boldsymbol{J})$ is one on which

$$\boldsymbol{N} \cdot \boldsymbol{\Omega} = 0, \tag{25}$$

where $\boldsymbol{N}$ is a vector with integer components and

$$\boldsymbol{\Omega} \equiv \frac{\partial H_0}{\partial \boldsymbol{J}} \tag{26}$$

is the vector of frequencies. In the rotating frame, Ω_ϕ changes sign at corotation from positive inside corotation to negative outside it. Hence to satisfy equation (25) with $N_z = 0$, the ratio N_r/N_ϕ has to rise from negative values inside corotation, through zero at corotation to positive values outside corotation. The best-known resonances of this class are the inner Lindblad resonance, $\boldsymbol{N} = (1, 0, -2)$, the ultraharmonic resonance $\boldsymbol{N} = (1, 0, -4)$, the corotation resonance $\boldsymbol{N} = (0, 0, 1)$ and the outer Lindblad resonance, $\boldsymbol{N} = (1, 0, 2)$. B16 examined the case $\boldsymbol{N} = (1, 1, 0)$, and we can exploit the formalism developed there by simply replacing $\overline{H}$ in the formulae of B16 by H_0.

Near a resonance, the angle variable

$$\theta_1' \equiv \boldsymbol{N} \cdot \theta \tag{27}$$

evolves slowly and we make a canonical transformation to new angle-action variables $(\theta', \boldsymbol{J}')$ that include this variable. We use the generating function

$$S'(\boldsymbol{\theta}, \boldsymbol{J}') = J_1' \boldsymbol{N} \cdot \theta + J_2' \theta_2 + J_3' \theta_3, \tag{28}$$

which ensures that equation (27) holds and makes $\theta_{2,3}' = \theta_{2,3}$. From $\boldsymbol{J} = \partial S/\partial \boldsymbol{\theta}$, we find

$$\begin{aligned} J_1 &= N_1 J_1' & & J_1' = J_1/N_1 \\ J_2 &= N_2 J_1' + J_2' & \leftrightarrow \quad & J_2' = J_2 - J_1 N_2/N_1 \\ J_3 &= N_3 J_1' + J_3' & & J_3' = J_3 - J_1 N_3/N_1. \end{aligned} \tag{29}$$

We Fourier expand the Hamiltonian in the new angle variables

$$H(\boldsymbol{\theta}', \boldsymbol{J}') = H_0(\boldsymbol{J}') + \sum_{\boldsymbol{k}\neq 0} \hat{h}_{\boldsymbol{k}} \mathrm{e}^{\mathrm{i}\boldsymbol{k}\cdot\boldsymbol{\theta}'}, \tag{30}$$

where $|\hat{h}_{\boldsymbol{k}}| \ll H_0$. The new actions have the equations of motion

$$\dot{\boldsymbol{J}}' = -\frac{\partial H}{\partial \boldsymbol{\theta}'} = -\mathrm{i}\sum_{\boldsymbol{k}} \boldsymbol{k}\hat{h}_{\boldsymbol{k}} \mathrm{e}^{\mathrm{i}\boldsymbol{k}\cdot\boldsymbol{\theta}'}. \tag{31}$$

Averaging these equations over the fast angles $\theta'_{2,3}$, we conclude that the actions $J'_{2,3}$ are effectively constant under the perturbation, so we need consider only the system's motion in the (θ'_1, J'_1) plane. This motion is governed by the Hamiltonian

$$H(\theta'_1, \boldsymbol{J}') = H_0(J'_1) + \sum_{n\neq 0} \hat{h}_n(J'_1) \mathrm{e}^{\mathrm{i}n\theta'_1}, \tag{32}$$

where $\hat{h}_n \equiv \hat{h}_{(n,0,0)}$ and we have omitted references to the constant actions $J'_{2,3}$. Since this a time-independent Hamiltonian, the motion occurs on the curve in the (θ'_1, J'_1) plane on which $H = I$, a constant. A good approximation to this motion can be obtained by Taylor expanding the functions of J'_1 in equation (32). However, before we do so we exploit the reality of H to write

$$H(\theta'_1, \boldsymbol{J}') \simeq H_0(J'_1) + 2\sum_n h_n(J'_1)\cos(n\theta'_1 + \psi_n), \tag{33}$$

where the h_n are the amplitudes and ψ_n are the phases of the complex variables $\hat{h}_n$. We expand H_0 and h_n to the second order in

$$\Delta \equiv J'_1 - J'_{01}, \tag{34}$$

where J'_{01} is the primed action of the resonant torus. Since a constant term in H can be discarded and we know that $\partial H_0/\partial J'_1 = 0$ on the resonant torus (equation 25), we replace H_0 by $\frac{1}{2}G\Delta^2$, where

$$G \equiv \frac{\partial^2 H_0}{\partial J'^2_1} = \frac{\partial \Omega'_1}{\partial J'_1}. \tag{35}$$

The Taylor series for $h_n(J'_1)$,

$$h_n(J'_1) = h_n^{(0)} + h_n^{(1)}\Delta + \tfrac{1}{2}h_n^{(2)}\Delta^2 + \cdots \tag{36}$$

cannot be simplified in this way, so the equation $H = I$ becomes

$$\begin{aligned} 0 = &\left(\frac{1}{2}G + \sum_n h_n^{(2)}\cos(n\theta'_1 + \psi_n)\right)\Delta^2 \\ &+ 2\left(\sum_n h_n^{(1)}\cos(n\theta'_1 + \psi_n)\right)\Delta \\ &+ \left(2\sum_n h_n^{(0)}\cos(n\theta'_1 + \psi_n) - I\right). \end{aligned} \tag{37}$$

In this approximation, we can determine $J'_1(\theta'_1)$ simply by solving the quadratic equation (37) for Δ given θ'_1. Given the oscillating value of J'_1 and the constants $J'_{2,3}$, we can recover the complete action-space coordinates from equations (29). In general, all three components of $\boldsymbol{J}$ oscillate but in such a way that H is to leading order constant.

If we retain only one value of n and neglect $h_n^{(1)}$ and $h_n^{(2)}$, equation (37) reduces to the energy equation of a pendulum and this is traditionally used to discuss resonant trapping (e.g. Chirikov 1979). Kaasalainen (1994) demonstrated the merit of retaining $h_n^{(1)}$ and $h_n^{(2)}$. B16 retained two values of n, but we shall find in the applications considered here that there is only one value of n to consider.

4.2 Action and angle of libration

The range through which θ'_1 oscillates is set by the condition that the quadratic for Δ has real roots:

$$\begin{aligned} \left[\sum_n h_n^{(1)}\cos(n\theta'_1 + \psi_n)\right]^2 \geq &\left(\tfrac{1}{2}G + \sum_n h_n^{(2)}\cos(n\theta'_1 + \psi_n)\right) \\ &\times\left(2\sum_n h_n^{(0)}\cos(n\theta'_1 + \psi_n) - I\right). \end{aligned} \tag{38}$$

When $G < 0$, as is the case at both OLR and CR, condition (38) is satisfied for the widest range of angles when $I < 0$ also, so the second bracket on the right is often positive. If I is less than a critical value $I_{\rm bot}$, the condition is satisfied but for no value of θ'_1 becomes by equality. Consequently, at no value of θ'_1 do the roots coincide, and the orbit is restricted to one root or the other. This is the regime of circulation. The two roots corresponds to circulation inside and outside the region of entrapment.

When I is larger than $I_{\rm bot}$, condition (38) is satisfied in a restricted range in θ'_1, and an orbit can transfer from one root to the other at the extremes of this range. This is the regime of libration. As I increases, the range shrinks and it vanishes at $I = I_{\rm top}$. When $I = I_{\rm top}$ the amplitude of libration vanishes.

In the case of the OLR we find that $G < 0$ and h_n vanishes for $n > 1$ and that $\psi_1 = \pi$. So when $h^{(1)}$ and $h^{(2)}$ are neglected, the libration condition is

$$I \leq 2h_1^{(0)}\cos(\theta'_1 + \pi). \tag{39}$$

Given that the h_n are by definition all non-negative, it follows that libration occurs around $\theta'_1 = \pi$. Hence, when $I = I_{\rm top} \simeq 2h_1^{(0)}$, equation (39) forces $\theta'_1 = \pi$, and the libration amplitude vanishes. Conversely, when $I = I_{\rm bot} \simeq -2h_1^{(0)}$ the libration amplitude becomes π. It follows that $I_{\rm bot}$ is the value of I for which condition (38) is an equality with the cosines set to -1, while $I_{\rm top}$ is the value of I at which equality is reached with the cosines equal to $+1$.

Each value of I in the range $I_{\rm bot} < I \leq I_{\rm top}$ corresponds to an action $\mathcal{J}$ that quantifies the extent to which a trapped orbit oscillates around the trapping torus. $\mathcal{J}$ is straightforwardly computed as

$$\mathcal{J} = \frac{1}{2\pi}\oint \mathrm{d}\theta'_1 J'_1(\theta'_1), \tag{40}$$

where the dependence of J'_1 on θ'_1 is obtained from equation (37). Since θ'_1 increases from its minimum to its maximum value with Δ given by the larger root of the quadratic (37) and returns to its minimum value with Δ given by the smaller root, $\mathcal{J}$ is given by the difference of the roots Δ integrated over the range of θ'_1.

The procedure for computing the actions of circulating orbits is very similar: one averages the relevant root $\Delta(\theta'_1)$ with respect to θ'_1 and then adds this average to the value of J'_1 for the perfectly resonant torus to obtain the value of J'_1 on the newly created torus.

On a trapped or nearly trapped orbit, θ'_1 is not an angle variable, although $\theta'_{2,3}$ are angle variables. Since the missing angle variable evolves linearly in time, it is

$$\vartheta(\theta'_1) = 2\pi\frac{\int_0^{\theta'_1}\mathrm{d}\theta'_1/\dot{\theta}'_1}{\oint \mathrm{d}\theta'_1/\dot{\theta}'_1}, \tag{41}$$

where from Hamilton's equation and equation (33) we have

$$\dot{\theta}'_1 = G\Delta + 2\sum_n \left(h_n^{(1)} + h_n^{(2)}\Delta\right)\cos(n\theta'_1 + \psi_n). \tag{42}$$

In this equation, Δ is by the quadratic equation (37) a function of θ'_1.

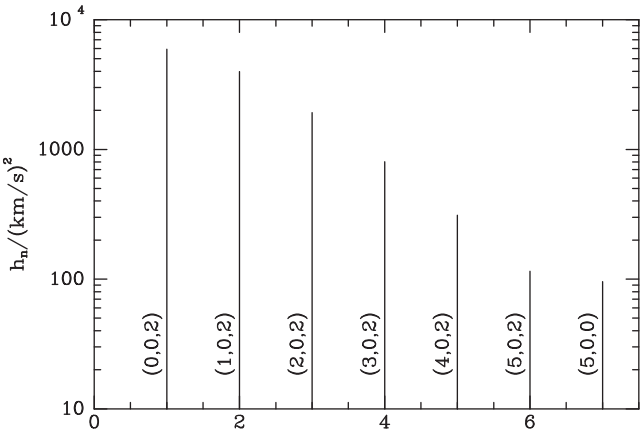

Figure 3. The amplitudes of the Fourier components of H on a torus that satisfies the condition for the OLR. The six largest terms all belong to a single sequence $\boldsymbol{k} = (j, 0, 2)$ for $j = 0, 1, \ldots$.

4.3 Impact of non-resonant terms

Above we neglected all non-resonant terms by averaging the equations of motion (31) over the fast angles. This procedure works extremely well when the tori are fitted to the full Hamiltonian rather than just a symmetric part of it because the fitting procedure can, in principle, reduce the non-resonant terms in the Fourier decomposition of H to arbitrarily small values. Unfortunately, in the present case the torus is fitted to the axisymmetric part of H and the variation of H over the fitted tori include significant non-resonant terms. We should include these terms in the perturbative treatment.

Fig. 3 illustrates this point by showing the values of the $h_{\boldsymbol{k}}$ for a torus on which the condition for the OLR is perfectly satisfied. The largest term is non-resonant, being proportional to $\cos 2\theta_\phi$. There follow a series of terms that are proportional to $\cos(n_r\theta_r + 2\theta_\phi)$. Of these terms only the largest, which has $n_r = 1$, is resonant. The impact of this term was computed above. Here, we compute the impact of the non-resonant terms.

It is convenient to work in the $(\boldsymbol{\theta}', \boldsymbol{J}')$ coordinate system in which, according to the theory of Section 4.1, J_2' and J_3' are constant, while J_1' obeys a pendulum equation. The non-resonant terms induce small oscillations in J_3' and slightly modify the pendulum motion of J_1'.

We consider first the largest non-resonant term, which is a particularly simple case because it has $n_r = 0$ and the only equation of motion affected by this term is that for J_3'. Moreover $\theta_3' = \theta_\phi$, so we may write

$$\frac{\mathrm{d}J_3'}{\mathrm{d}\theta_3'} = \frac{\dot{J}_3'}{\Omega_3'} = -\frac{1}{\Omega_3'}\frac{\partial H}{\partial \theta_3'}. \tag{43}$$

Integrating this equation, it follows that

$$J_3'(\theta_3') = \overline{J_3'} - \frac{2h_{002}}{\Omega_3'}\cos(2\theta_3' + \psi_{002}), \tag{44}$$

where $\overline{J_3'}$ denotes the average value of J_3', which we interpret to be value of J_3' for the perfectly resonant torus. It is perhaps worth noting that equation (44) could have been obtained by requiring that at any point on the orbit the change in the unperturbed Hamiltonian,

$$\delta H_0 = \frac{\partial H_0}{\partial J_3'}\,\delta J_3', \tag{45}$$

cancel the numerical value of the perturbing Hamiltonian.

In a similar vein, the contributions of the other non-resonant terms to the equations of motion are

$$\begin{aligned}
\delta J_1' &= -\int \frac{\mathrm{d}\theta_3'}{\Omega_3'}\frac{\partial \delta H}{\partial \theta_1'} \\
&= -\int \frac{\mathrm{d}\theta_3'}{\Omega_3'}\frac{n/N_1}{2 - nN_3/N_1}\frac{\partial \delta H}{\partial \theta_3'} \\
&= -\frac{2nh_{n02}}{\Omega_3'(2N_1 - nN_3)}\cos(n\theta_r + 2\theta_\phi + \psi_{n02}) \\
\delta J_3' &= -\int \frac{\mathrm{d}\theta_3'}{\Omega_3'}\frac{\partial \delta H}{\partial \theta_3'} \\
&= -\frac{2h_{n02}}{\Omega_3'}\cos(n\theta_r + 2\theta_\phi + \psi_{n02}).
\end{aligned} \tag{46}$$

When we set $n = 0$ and $N_3 = 2$, these equations are equivalent to equation (44) for the change induced by the largest perturbation.

For each relevant value of $n = 2, 3, \ldots$ we increment J_1' and J_3' by the amounts given in equation (46) from the values yielded by the resonant theory of Section 4.1.

4.4 Resonant or non-resonant theory?

The point of the pendulum equation is that it yields an accurate representation of the non-uniform evolution of the resonant angle $\theta_1' = \boldsymbol{N}\cdot\boldsymbol{\theta}$. The equation's weakness is that it derives its data from the immediate vicinity of the perfectly resonant torus. Specifically, we use with it values of G and the resonant Fourier amplitudes h_n that were obtained from Taylor series, but the employed values of the non-resonant amplitudes $h_{\boldsymbol{k}}$ are simply those of the perfectly resonant torus. Near that torus, the pendulum equation provides accurate results, but as we move away, errors arising from stale values of $h_{\boldsymbol{k}}$ grow. Meanwhile, as we move deeper into the region of circulation, the motion of the resonant angle becomes faster and more uniform. At some point, it becomes advantageous to abandon the pendulum equation and simply apply equations (46), but now including *all* the $h_{\boldsymbol{k}}$ rather than just the non-resonant terms, and using the values of $h_{\boldsymbol{k}}$ and $\boldsymbol{\Omega}$ for the current torus rather than for the perfectly resonant torus.

5 EXAMPLES

In this section, we show results obtained when the formalism of the last section is applied to the Hamiltonian associated with the model Galactic potential of Section 3. In Fig. 4, the colour scale and white contours show the value of the axisymmetric Hamiltonian $H_0(\boldsymbol{J})$ through a significant part of action space. At a given (small) value of J_r, H_0 peaks at the value of J_ϕ associated with corotation. This ridgeline in H_0 corresponds to the fact that in a rotating frame the effective potential $\Phi(R, z) - \frac{1}{2}\omega_{\mathrm{p}}^2 R^2$ has the structure of a volcano in that it falls away from a roughly circular rim in the vicinity of corotation into the crater on one side and down towards the flat lands on the other (e.g. Binney & Tremaine 2008, fig. 3.14). Fig. 4 is computed for vertical action $J_z = 0.0025\,\mathrm{kpc^2\,Myr^{-1}}$, which typically lets solar-neighbourhood orbits to reach $z \sim 0.27\,\mathrm{kpc}$. However, the diagram computed for $J_z = 0.025\,\mathrm{kpc\,Myr^{-1}}$, which lets stars to reach $z \sim 0.97\,\mathrm{kpc}$, is virtually indistinguishable. Thus, the response of stars to the bar will not depend on whether they belong to the thin or thick disc.

Two black ladder-like structures are evident in Fig. 4. The left-hand ladder marks the region within which stars are trapped at corotation, while the right-hand ladder marks the region of entrapment by the OLR. The line down the centre of each ladder marks

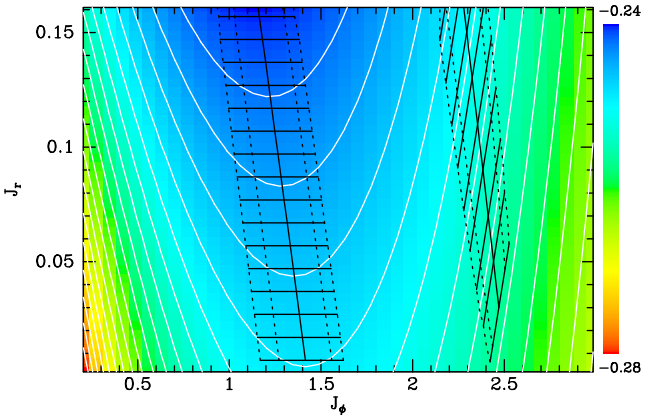

Figure 4. The colour scale and white contours give the value of the axisymmetric Hamiltonian H_0 in the (J_ϕ, J_r) plane at $J_z = 0.0025\,\mathrm{kpc}^2\,\mathrm{Myr}^{-1}$. The zones of entrapment at corotation (centre) and at the OLR (right) are marked by black ladder-like structures. A full line down the middle of each structure joins unperturbed tori on which the resonance condition is satisfied. The dashed lines on each side mark the boundaries of the region within which orbits are trapped computed from perturbation theory. The actions of trapped orbits oscillate along lines parallel to the rungs of each ladder. Along the lines on which the resonance condition is satisfied, the rungs are tangent to contours of constant H_0. The shell orbit through the Sun sits near the x-axis at $J_\phi = 1.96\,\mathrm{kpc}^2\,\mathrm{Myr}$.

the tori on which the relevant resonance condition is exactly satisfied. The shorter lines or 'rungs' that cross this central line are the tangents to the contours of constant H_0 where they cross the central line. During libration the locations of orbits in the (J_ϕ, J_r) plane oscillate parallel to these rungs. Each side of the ladder is marked by two parallel lines. The distance across a ladder between the inner lines measures the maximum amplitude of libration of trapped orbits, which is simply the value of the libration action $\mathcal{J}$ obtained by setting $I = I_{\rm bot}$ in the pendulum formulae. The outer lines indicate the furthest excursions Δ of trapped orbits from the actions of the underlying perfectly resonant orbit. Within the phase space associated with the gap between the inner and outer lines there are orbits that librate and orbits that circulate. These orbits are all best computed with resonant perturbation theory, while outside this region non-resonant theory is usually more reliable.

5.1 Trapping at the OLR

Fig. 5 shows a typical orbit trapped at the OLR. The red curve shows the trajectory yielded by perturbation theory, while the black curve shows the trajectory obtained by numerically integrating the full equations of motion from a single phase-space point on the red trajectory. Since perturbation theory yields a close approximation to an orbit, starting the black trajectory from a different point makes very little difference to the figure.

Fig. 6 is a surface of section $\phi = z = 0$ at $J_z = 0.0025\,\mathrm{kpc}^2\,\mathrm{Myr}^{-1}$ and $J_3' = 2.17\,\mathrm{kpc}^2\,\mathrm{Myr}^{-1}$. The full curves are cross-sections through tori in the axisymmetric Hamiltonian H_0 obtained by torus mapping (Binney & McMillan 2016). The condition for resonance at the OLR is satisfied on the middle torus, and the tori generating the outermost and innermost curves are the tori that perturbation theory predicts will bound the region of entrapment.

The points in Fig. 6 are consequents of seven orbits integrated with the full equations of motion from initial conditions on the resonant torus. The consequents of any given orbit lie on a curve

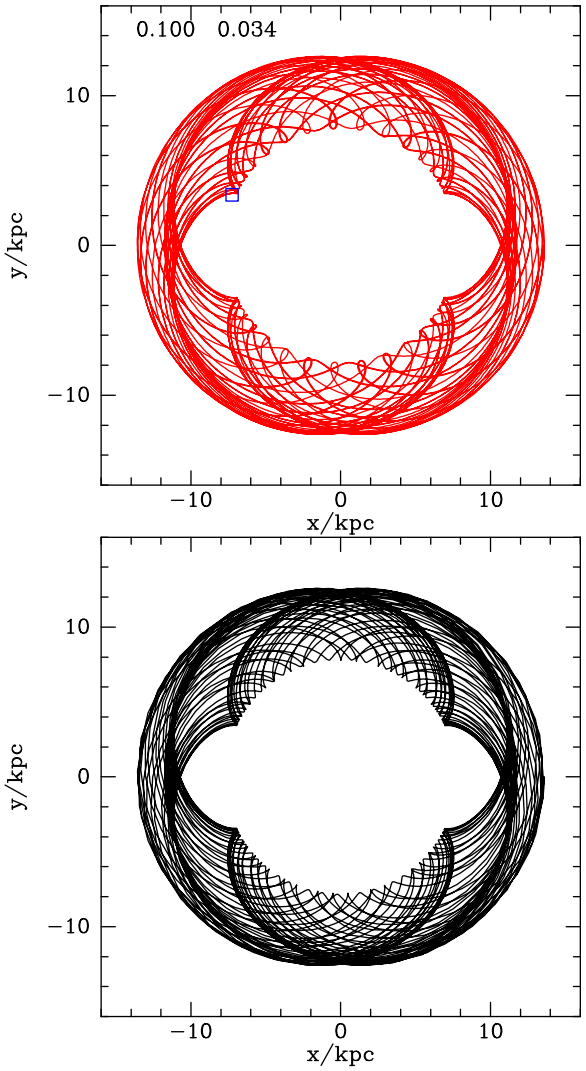

Figure 5. In red an orbit trapped at OLR generated with perturbation theory. In black, the same orbit integrated numerically. For this orbit $J_z = 0.0025\,\mathrm{kpc}^2\,\mathrm{Myr}^{-1}$, $J_3' = 2.17\,\mathrm{kpc}^2\,\mathrm{Myr}^{-1}$, $I = 0.6 I_{\rm bot}$ and $\mathcal{J} = 0.034\,\mathrm{kpc}^2\,\mathrm{Myr}$. The orbit reaches distance $|z| = 0.43\,\mathrm{kpc}$ from the plane. The underlying resonant orbit has $J_r = 0.1\,\mathrm{kpc}^2\,\mathrm{Myr}^{-1}$. The black square in the upper panel shows the likely location of the Sun.

because these are quasi-periodic orbits. But for only two orbits does this curve resemble the cross-section of a torus generated by TM. It is evident that on the orbits that gave rise to the innermost and outermost sets of consequents the resonant angle θ_1' circulates, while in the intervening five orbits θ_1' librates. We see that the boundaries of the region of entrapment are quite accurately predicted by perturbation theory. The cross-sections of the tori almost coincide at small R but this is an illusion: the tori have distinct values of J_ϕ, with the consequence that at a given R they are well separated in v_ϕ.

The upper panel of Fig. 7 shows the same surface of section as Fig. 6 but with the cross-sections through tori of H_0 now shown in broken blue lines. The full black curves in Fig. 7 are cross-sections through tori computed with the perturbation theory presented above. The points are consequents obtained by integrating the full equations of motion from one phase-space point on each full curve. The orbit shown in Fig. 5 produces consequents that lie just outside the outermost of the curves of trapped orbits. The agreement between

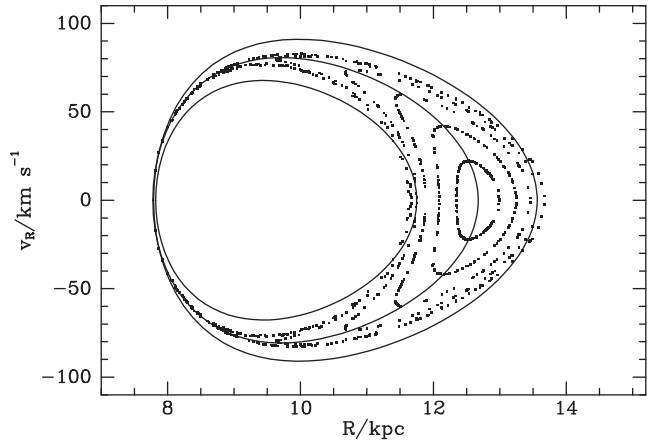

Figure 6. A surface of section $\phi = z = 0$. Each curve is a cross-section through a torus of the axisymmetric Hamiltonian H_0. The resonance condition for the OLR is satisfied on the middle torus. The points are the consequents of orbits integrated in the full barred Hamiltonian from points on the resonant torus.

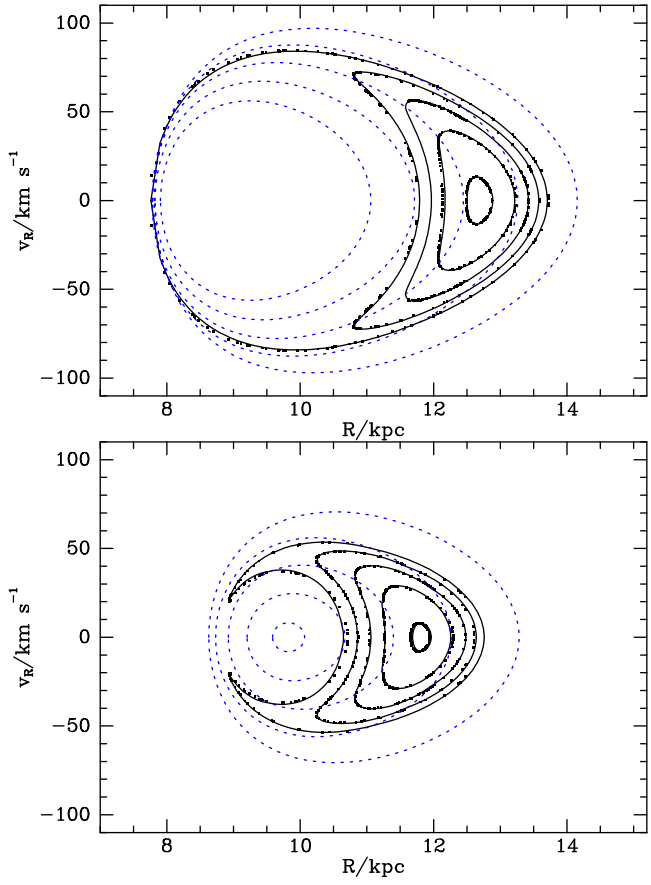

Figure 7. Two surfaces of section $\phi = z = 0$. The full black curves are cross-sections through tori constructed perturbatively. The points are consequents on orbits started from a point on each of these curves. The broken blue curves show cross-sections through unperturbed tori like those used to construct the perturbed tori. The upper panel is for the case that the underlying resonant orbit has $J_r = 0.1\,\mathrm{kpc^2\,Myr^{-1}}$, while the lower panel is for $J_r = 0.035\,\mathrm{kpc^2\,Myr^{-1}}$. In the latter case the trapping region approaches $J_r = 0$, so the innermost broken blue curve is very small. In the upper panel the lowest value of $I = 1.05I_{\rm bot}$ so the orbit generating the outermost curve circulates, while in the lower panel the smallest value of $I = 0.98I_{\rm bot}$ so the outermost orbit librates.

the points and the full curves is excellent, both for the four orbits that librate and for the fifth, circulating orbit, on which $I = 1.05I_{\rm bot}$.

The lower panel of Fig. 7 is similar to the upper panel but for the case that the perfectly resonant torus has $J_r = 0.035\,\mathrm{kpc^2\,Myr^{-1}}$. The orbit with the maximum amplitude of libration around this resonant torus comes close to the torus $J_r = 0$ in the course of its libration, so the innermost blue curve is small.

To obtain the results from perturbation theory plotted in Fig. 7, one has to be able to predict $(\boldsymbol{x}, \boldsymbol{v})$, given arbitrary values $(\boldsymbol{\theta}, \boldsymbol{J})$. Given a value of $\boldsymbol{J}$, the associated torus is constructed by interpolation on a grid of 10 tori that lie along the edge of a rectangle five grid points wide and two grid points high in the (J_1', J_3') plane. It proves advantageous for the grid to be uniformly spaced in $\sqrt{J_r}$ rather than in J_r as the worst interpolation errors arise near the 'skinny' torus that lies on the J_ϕ axis in Fig. 4. The axisymmetric tori that generated the broken blue curves in Fig. 7 lie along the long axis of the rectangle and were obtained by interpolating between pairs of tori that have the same value of J_1'. Their near-uniform increase in radius reflects their uniform spacing in $\sqrt{J_r}$.

The area enclosed by each broken curve in Fig. 7 is proportional to the value of J_r on the corresponding torus. Thus, in the upper panel, all these tori have non-negligible values of J_r, but in the lower panel, associated with a resonant orbit that has less radial action by a factor of $\sim$3, the innermost broken blue curve has a very small area and thus corresponds to an essentially circular orbit. The area inside each full black curve is proportional to the value of the resonant action $\mathcal{J}$ (equation 40). At the centre of the island of full curves would lie the single consequent generated by the closed trapped orbit $\mathcal{J} = 0$, which we can obtain by setting $I = I_{\rm top}$.

5.2 Trapping at corotation

Unfortunately, a slight adjustment to the theory of Section 4 is required before we apply it to the corotation resonance because at corotation the slow angle is $\boldsymbol{N}\cdot\boldsymbol{\theta} = \theta_\phi$, so if equations (29) are to apply we must re-order our unperturbed angles and actions such that

$$\begin{aligned}(\theta_1, J_1) &= (\theta_\phi, J_\phi)\\ (\theta_3, J_3) &= (\theta_r, J_r).\end{aligned} \tag{47}$$

This done, the previous analysis is valid with $\boldsymbol{N} = (1, 0, 0)$, with the result that we do not need to distinguish between $\boldsymbol{J}$ and $\boldsymbol{J}'$. The impact of the non-resonant terms is now as follows. A term changes the actions by

$$\begin{aligned}\delta J_r &= \int \mathrm{d}t\, \dot{J}_r = \int \frac{\mathrm{d}\theta_r}{\Omega_r}\dot{J}_r\\ &= -\frac{2h_{20n}}{\Omega_r}\cos(n\theta_r + 2\theta_\phi + \psi_{20n})\\ \delta J_\phi &= \int \mathrm{d}t\, \dot{J}_\phi = \int \frac{\mathrm{d}\theta_r}{\Omega_r}\dot{J}_\phi\\ &= -\frac{4h_{20n}}{n\Omega_r}\cos(n\theta_r + 2\theta_\phi + \psi_{20n}).\end{aligned} \tag{48}$$

The resonant term in the Hamiltonian $h_{200}\cos(2\phi + \psi)$ has $\psi = \pi$, so trapped orbits librate around $\theta_\phi = \pi/2$, which corresponds to a point on the minor axis of the potential – in the limit $J_r \to 0$ this coincides with the Lagrange point L_4. Fig. 8 shows a trapped orbit, in black as computed by integration of the full equations of motion and in red as computed from perturbation theory after reflection in the x-axis to avoid overplotting the numerically integrated version. This orbit has a relatively large amplitude of libration, so it reaches

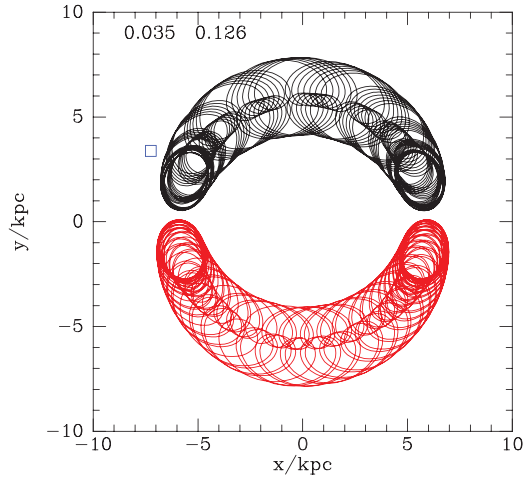

Figure 8. An orbit trapped at corotation plotted in black by integration of the full equations of motion and in red using perturbation theory after reflection in the x-axis. The orbit, which reaches $z = 270$ pc, has $J_r = 0.035\,\mathrm{kpc^2\,Myr^{-1}}$ and action of libration is $\mathcal{J} = 0.126\,\mathrm{kpc^2\,Myr^{-1}}$. The blue square shows the likely location of the Sun.

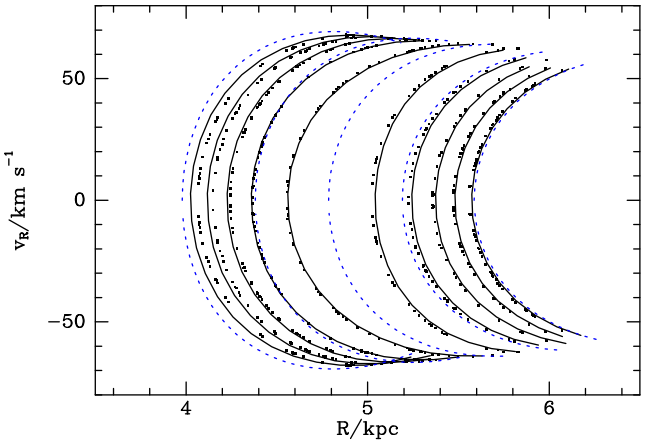

Figure 9. Surface of section $\phi = \pi/2$, $z = 0$ at $J_r = 0.035\,\mathrm{kpc^2\,Myr^{-1}}$, $J_z = 0.0025\,\mathrm{kpc^2\,Myr^{-1}}$. The full black curves and the points are for five orbits trapped at corotation, the curves being computed with perturbation theory and the points being consequents from numerically integrated orbits launched from one point on each curve. The actions of libration are $\mathcal{J} = 0.140, 0.098, 0.066, 0.037, 0.011\,\mathrm{kpc^2\,Myr^{-1}}$. The broken blue curves are computed from the three tori of H_0 that were used as the basis of interpolation when computing the full black curves.

all the way to the long axis of the bar. In fact, this orbit supports the bar quite strongly because the star lingers at the turning points of its libration, when it lies near the x-axis. The loops along the orbit's inner and outer crescents are clearly arise from radial oscillations that have a much shorter period than the period of libration. The only significant difference between the red and black versions of the orbit is a small change in the ratio of these periods.

Fig. 9 is a surface of section $\phi = \pi/2, z = 0, \dot\phi > 0$ for orbits with the same radial and vertical actions $[(J_r, J_z) = (0.035, 0.0025)\,\mathrm{kpc^2\,Myr^{-1}}]$ as the orbit shown in Fig. 8. The full curves are the predictions of perturbation theory for five values of I, while the data points were generated by integrating the full equations of motion from a single point on each of the perturbed tori. Each orbit generates two crescents: the orbit with the largest libration amplitude generates the crescents on the extreme left and the extreme right, the orbit with the second largest libration amplitude generates the next two crescents in, and so on. As is to be expected, the agreement between the data points and the full curves deteriorates as the amplitude of libration increases.

Since we have imposed the requirement $\dot\phi > 0$, all points arise from times at which the star lies inside its guiding-centre radius and thus is moving progradely in the corotating frame. That is, all points arise not too far from pericentre. If the restriction $\dot\phi > 0$ is lifted, each crescent is complemented by an oppositely directed crescent so each orbit contributes two ellipses to the diagram, one centred on smaller radii than the other. The figure is then too busy to be helpful.

The broken blue curves in Fig. 9 show the points generated by three tori of H_0 constructed by interpolation along the centre of the 3×2 grid of tori from TM that underpins the construction of the non-axisymmetric tori. Both the data points and the full curves track these broken curves to a remarkable extent. However, in an axisymmetric potential each orbit would generate only *one* crescent, that associated with its angular momentum. In the non-axisymmetric potential, orbits generate two crescents because they cross the minor axis with one of two values of J_ϕ. The alignment of the full and broken curves signifies that the angular momentum with which a star returns to the minor axis is independent of the phase of its radial oscillations.

5.2.1 *Circulating orbits*

When TM fits tori to the full Hamiltonian, as in B16, everything one needs to know about an orbit that circulates rather than librates can be obtained directly from TM. Here, however, TM fits tori to only the axisymmetric part of the Hamiltonian, so perturbation theory is required to obtain a good fit to an orbit that circulates – in fact, the orbit can be significantly non-axisymmetric. Fig. 10 illustrates this point by showing orbits that have slightly too much (upper panel) and slightly too little (lower panel) angular momentum to be trapped by the corotation resonance. Both orbits are far from axisymmetric. As in Fig. 8, the black curves show the orbits obtained by direct integration of the equations of motion and the red curves show the orbits obtained with perturbation theory. The main difference between the black and red curves is the spacing between the loops to which radial oscillations give rise: along the black curve in the upper panel the loops are closer together, indicating that Ω_r/Ω_ϕ lies close to an integer, whereas along the red curve the loops are more clearly separated indicating a value of Ω_r/Ω_ϕ that lies less close to an integer.

Fig. 11 shows a surface of section. The orbit plotted in the upper panel of Fig. 10 produces the complete circuit of consequents on the right. The curve on which they lie was computed with perturbation theory. To set the context, we show on the left of this surface of section the consequents and invariant curves of two orbits with the same values of J_r and J_z but with $I > I_{\rm bot}$, so they librate. For these orbits, as in Fig. 9, we only show consequents associated with $\dot\phi > \omega_{\rm p}$, whereas for the circulating orbit we show consequents for both signs of $\dot\phi - \omega_{\rm p}$. This is why the invariant curve of the circulating orbit closes on itself, whereas the invariant curves of the other two orbits form pairs of crescents, one for each of the two values of angular momentum at which the star crosses the bar's minor axis. The broken blue curves show cross-sections through five axisymmetric tori located along the central spine of the 5×2 grid of tori from TM that formed the basis for interpolation. The broken blue curve on the right, associated with the largest angular momentum, keeps quite close to the black invariant curve of the circulating orbit, indicating that as the latter passes the minor axis,

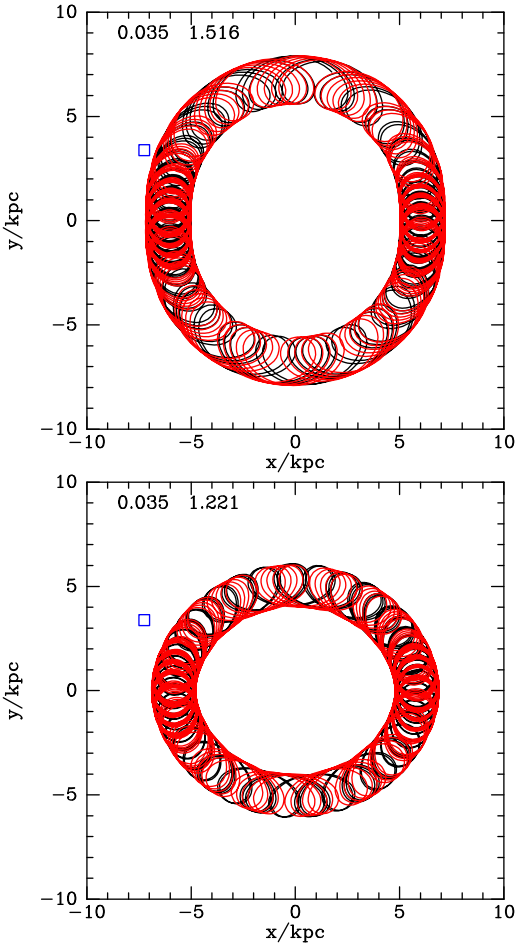

Figure 10. Orbits that circulate just outside (top) and inside (bottom) corotation. The colour scheme is that of Fig. 8. The upper orbit has extended angular-momentum action $J_\phi = 1.52\,\mathrm{kpc^2\,Myr^{-1}}$, while the lower orbit has $J_\phi = 1.22\,\mathrm{kpc^2\,Myr^{-1}}$. Both orbits have $(J_r, J_z) = (0.035, 0.0025)\,\mathrm{kpc^2\,Myr^{-1}}$.

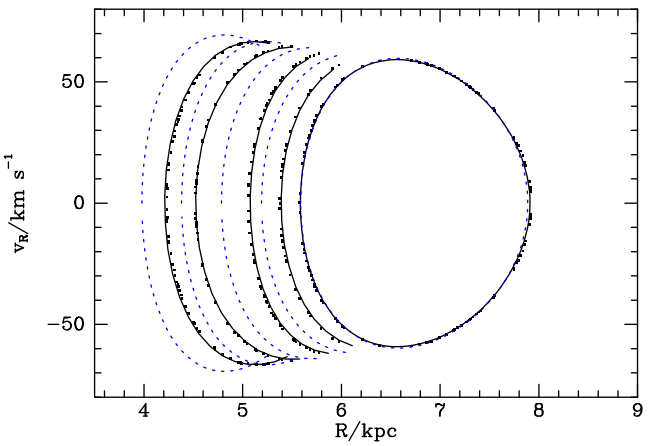

Figure 11. In this surface of section $\phi = \pi/2$, $z = 0$ the circulating upper orbit of Fig. 10 generates the complete circuit of consequents on the right. The full curve was computed from perturbation theory. Also shown on the left are the consequents and invariant curves of two librating orbits that differ from the circulating orbit in having $I > I_{\mathrm{bot}}$. The broken blue curves show the cross-sections of tori produced by TM that provided the basis for perturbation theory.

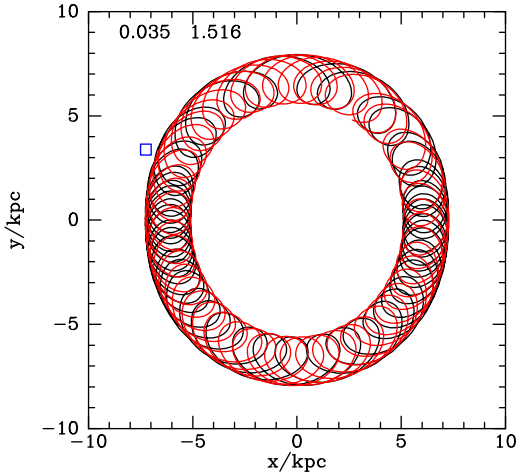

Figure 12. The orbit shown in the upper panel of Fig. 10 computed using non-resonant perturbation theory. The general shape of the orbit is correctly reproduced but the orbit fails to linger near the x-axis.

its angular momentum lies in a narrow range. This does not imply, however, that the orbit's angular momentum is nearly constant: near the major axis it has substantially more angular momentum.

The above reconstruction of a circulating orbit was obtained from the pendulum equation. As such it relies on the determination of the Fourier coefficients h_k on the perfectly resonant torus, which is at some distance from it in phase space.

As was noted in Section 4.4, when an orbit is obtained from resonant perturbation theory, one is using Fourier coefficients of H that are becoming increasingly stale as one progresses away from the region of entrapment. At some point, it becomes expedient to adopt non-resonant perturbation theory, for then the Fourier coefficients employed are computed locally, on the unperturbed tori over which the orbit is actually ranging. The analytic work of Monari, Famaey & Siebert (2016) is based on this type of perturbation theory.

The red curve in Fig. 12 shows the orbit that circulates just outside the region of entrapment by corotation as obtained from non-resonant perturbation theory, with the black curve as usual showing the result of direct numerical integration. We see that non-resonant perturbation theory recovers the shape of the orbit well, but comparison with the upper panel of Fig. 10, which shows the same orbit computed with resonant perturbation theory, reveals a failure to recover the way the orbit lingers along the x-axis. This is a natural consequence of the key approximation of non-resonant theory, namely that the unperturbed angles evolve uniformly in time. Further from the boundary of the region of entrapment, the non-uniform evolution of the unperturbed angle variables becomes less marked and non-resonant perturbation theory comes into its own.

In conclusion, resonant perturbation should be used both inside and close to the region of entrapment, while non-resonant theory should be used elsewhere.

5.3 Trapping at the ILR

To obtain orbits trapped at the inner Lindblad resonance, the code described in Appendix A should be used to construct an instance of `resTorus_L` with the resonant vector set to $\boldsymbol{N} = (1, 0, -2)$. In contrast to the CR and OLR, at the ILR G proves positive while ψ_N vanishes. As a consequence, libration is still around $\theta_1' = \pi$ but

now the torus with $I = I_{\rm bot}$ has vanishing libration amplitude while maximum libration amplitude is attained at $I = I_{\rm top} > I_{\rm bot}$. Values of I smaller than $I_{\rm bot}$ are now forbidden, while values larger than $I_{\rm top}$ correspond to circulating orbits.

Examples of orbits trapped at the ILR will be given in a forthcoming publication that focuses on resolving difficulties that the current version of TM encounters with orbits that have small J_r and large $\mathcal{J}$.

6 STRUCTURE OF LOCAL VELOCITY SPACE

Now we use our non-axisymmetric tori to examine the structure of the velocity distribution of solar-neighbourhood stars. This exercise illustrates both the inconvenience of orbit-based models of galaxies and the relative strength of torus modelling among orbit-based techniques. We define $U = v_{R\odot} - v_R$ and $V = v_\phi - v_{\phi\odot}$, so the Sun is at (0, 0), U increases with motion towards the Galactic Centre and V is the amount by which the star's motion in the direction of Galactic rotation exceeds that of the Sun. We assume that $(v_{R\odot}, v_{\phi\odot}) = (-11, v_{\rm c} + 12)\,{\rm km\,s^{-1}}$ (Schönrich, Binney & Dehnen 2010). For reasons that will become apparent, most results are presented for pattern speed $\omega_{\rm p} = 0.038\,{\rm Myr^{-1}}$.

6.1 Orbit-based modelling

When one wishes to compute the density or the velocity distribution at a given point in a model, it is enormously desirable to be in possession of an algorithm that computes $(\boldsymbol{\theta}, \boldsymbol{J})$, given $(\boldsymbol{x}, \boldsymbol{v})$, for then the density at position $\boldsymbol{v}$ in velocity space is simply $f(\boldsymbol{J})$ and the density can be recovered by integrating over $\boldsymbol{v}$. For an axisymmetric model, or a triaxial model that has zero pattern speed, we can use the Stäckel Fudge (Binney 2012a; Sanders & Binney 2015) for this purpose, but the Fudge has yet to be generalized to systems with rotating non-axisymmetric potentials. Algorithms for non-axisymmetric systems that have been used with some success are those of Dehnen (1999) and Monari et al. (2016). Dehnen (1999) evaluated $f(\boldsymbol{x}, \boldsymbol{v})$ by integrating an orbit from $(\boldsymbol{x}, \boldsymbol{v})$ backwards in time while the bar amplitude was reduced to zero, and then evaluated f at the computed location in the axisymmetric model. Monari et al. (2016) computed $f(\boldsymbol{x}, \boldsymbol{v})$ in essentially the same way except they followed orbits backwards analytically using non-resonant perturbation theory in axisymmetric angle-action coordinates. These algorithms rely on the adiabatic invariance of $\boldsymbol{J}$ and consequently fail when resonant trapping is important.

Given the lack of robust algorithms for computing $(\boldsymbol{\theta}, \boldsymbol{J})$ from $(\boldsymbol{x}, \boldsymbol{v})$ in rotating, non-axisymmetric potentials, nearly all modelling of non-axisymmetric systems (and much modelling of axisymmetric ones too) has been orbit based in the sense that one finds orbits and assigns them weights such that available observational data are consistent with the values predicted by the weighted averages of the orbits. The classic technique is that of Schwarzschild (1979) but important advances have recently made with the 'Made-to-Measure' (M2M) technique proposed by Syer & Tremaine (1996) and developed by de Lorenzi et al. (2007), Dehnen (2009), Long & Mao (2010) and Morganti & Gerhard (2012) among others.

The Schwarzschild and M2M techniques differ in (i) how weights are assigned and (ii) how orbits are used: del for each orbit M2M integrates orbits in parallel and for each orbit holds $(\boldsymbol{x}, \boldsymbol{v})$ for only a single time, whereas Schwarzschild integrates orbits in series and for each orbit retains $(\boldsymbol{x}, \boldsymbol{v})$ at a large number of times. Hence, Schwarzschild uses orbits as time series, and computes densities by summing the time intervals during which each star is in a small volume around the point at which the density is required. If orbits are replaced by tori, it becomes easier to compute the density because one then has analytic formulae for $\boldsymbol{x}(\boldsymbol{\theta})$ and $\boldsymbol{v}(\boldsymbol{\theta})$, so one can solve for the angles (if any) $\boldsymbol{\theta}$ at which the torus visits a given location and evaluate the velocities with which the visits occur. This approach underlies the code for chemodynamical evolution used by Schönrich & McMillan (2017), and also the analysis of data from the LAMOST survey (Deng et al. 2012) presented by Wang et al. (2017). Our non-axisymmetric, sometimes resonantly trapped, tori allow us the extend this technique to the non-axisymmetric problem posed by the solar neighbourhood.

The general plan is to compute tori for a grid in action space and find the velocities (if any) at which each torus visits the Sun. Then the density of the corresponding cells in the UV plane is incremented by

$$\frac{f(\boldsymbol{J})}{f_{\rm s}(\boldsymbol{J})}\frac{\partial(\boldsymbol{v})}{\partial(\boldsymbol{J})}, \tag{49}$$

where $f_{\rm s}$ is the sampling density that is defined by the grid. The Jacobian, which converts from density in action space to density in velocity space, is provided by TM. Indeed with $(\boldsymbol{x}, \boldsymbol{v})$ denoting Cartesian phase-space coordinates and S the generating function of the canonical transformation to angle-action coordinates,

$$\boldsymbol{\theta} = \frac{\partial S}{\partial \boldsymbol{J}} \text{ and } \boldsymbol{v} = \frac{\partial S}{\partial \boldsymbol{x}}, \tag{50}$$

so

$$\left.\frac{\partial \boldsymbol{v}}{\partial \boldsymbol{J}}\right|_{\boldsymbol{x}} = \frac{\partial^2 S}{\partial \boldsymbol{J}\partial \boldsymbol{x}} = \left.\frac{\partial \boldsymbol{\theta}}{\partial \boldsymbol{x}}\right|_{\boldsymbol{J}}. \tag{51}$$

Taking determinants it follows that

$$\frac{\partial(\boldsymbol{v})}{\partial(\boldsymbol{J})} = 1\Big/\frac{\partial(\boldsymbol{x})}{\partial(\boldsymbol{\theta})}. \tag{52}$$

TM does not directly provide the Jacobian on the right because it uses cylindrical polar coordinates. So it provides

$$\frac{\partial(R,z,\phi)}{\partial(\boldsymbol{\theta})} = \frac{\partial(\boldsymbol{x})}{\partial(\boldsymbol{\theta})}\frac{\partial(R,z,\phi)}{\partial(\boldsymbol{x})} = \frac{\partial(\boldsymbol{x})}{\partial(\boldsymbol{\theta})}\frac{1}{R}. \tag{53}$$

6.2 Orbits trapped at corotation

Each point in Fig. 13 shows the velocity with which a torus visits the Sun-like location $R_0 = 8\,{\rm kpc}$ $\phi = 155\,{\rm deg}$. We plot in red visits by tori that are not resonantly trapped, and in blue or black visits by tori that have been trapped by corotation. If a torus reaches the Sun, it usually does so at four distinct velocities, two with $v_z > 0$ and two with $v_z < 0$. In Fig. 13, we show only visits with $v_z > 0$. Then the plot should contain two visits per torus, one on the left and one on the right of a roughly horizontal line. In the region of entrapment at the bottom of the figure, the left-hand visits have been coloured black and the right-hand ones coloured blue. As the action of libration $\mathcal{J}$ diminishes, the left- and right-hand points converge on the rather bare space where the black and blue points approach one another. This bare region arises because the tori have been sampled uniformly in I: the region can be eliminated by sampling more densely at small values of $|I|$.

The dots in Fig. 13 are arranged in rings because the tori were computed on a grid in action space: for $0 \le n < N$, the grid in J_r is defined by

$$J_{r,n} = \left[\sqrt{J_{r\,\rm min}} + \frac{n}{N}\sqrt{J_{r\,\rm max}}\right]^2 \tag{54}$$

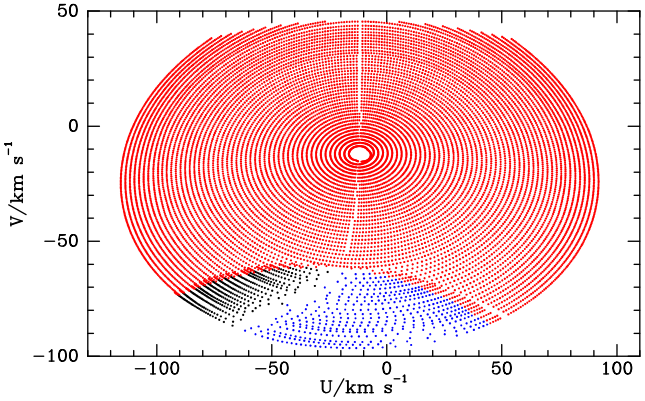

Figure 13. Each dot shows a velocity (U, V) at which a torus visits the Sun-like location $(R, z, \phi) = (8\,\mathrm{kpc}, 10\,\mathrm{pc}, 155^\circ)$. Points contributed by circulating tori are plotted in red while points contributed by tori trapped at corotation are plotted in blue/black. The bar's pattern speed is $0.038\,\mathrm{Myr}^{-1}$, 6850 tori contribute to the plot, and on the outermost red ellipse $J_r = 0.12\,\mathrm{kpc}^2\,\mathrm{Myr}^{-1}$.

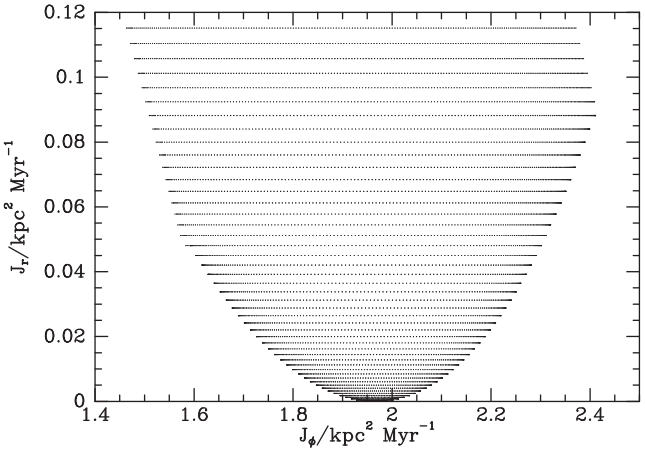

Figure 14. The distribution in action space of the tori that generated the red dots in Fig. 13. The parabolic shape at the base is defined by the requirement to be at apocentre or pericentre at the Sun. The clip off the top right corner is to avoid orbits trapped by the OLR. Similarly, the upper left edge is defined by avoidance of orbits trapped by the CR. Note the increased density of dots at the ends of each horizontal line and the increasing density of lines towards the base.

with $J_{r\,\mathrm{min}} = 0.0002\,\mathrm{kpc}^2\,\mathrm{km\,s}^{-1}$, $J_{r\,\mathrm{max}} = 0.12\,\mathrm{kpc}^2\,\mathrm{km\,s}^{-1}$ and $N = 50$. Fig. 14 shows the grid points in action space. By making the grid points uniform in $\sqrt{J_r}$, we ensure a near uniform distribution of rings in velocity space. Choosing grid points in J_ϕ is challenging because one wants to obtain points near the line $U = v_{R\odot}$. In the lower part of Fig. 13 and in an axisymmetric system, these points would correspond to visits of stars with low J_ϕ that reach the Sun at apocentre, while in the upper portion of the diagram the points correspond to visits at pericentre by stars with large J_ϕ. In a non-axisymmetric potential the situation is more complex, but the general idea holds. So for given J_r we compute the values of the generalized angular momentum J_ϕ of visits at apocentre (J_{apo}) and at pericentre (J_{peri}) and distribute our grid points between these lower and upper bounds on J_ϕ. We need grid points closely spaced near the limiting values because as $U \to v_{R\odot}$ the Jacobian in equation (49) diverges. Specifically, we take

$$J_{\phi,k} = \frac{1}{2}\left[J_{\mathrm{peri}} + J_{\mathrm{apo}} - (J_{\mathrm{peri}} - J_{\mathrm{apo}})\cos((k+\frac{1}{2})\pi/K)\right] \qquad (55)$$

for $0 \le k < K$ in integer steps. Then the divergence in the Jacobian is cancelled by a matching divergence in the sampling density f_{s} that reflects divergence of the density of grid points as $U \to v_{R\odot}$, which is just about visible in Fig. 14.

Fig. 13 reveals that this strategy has not been entirely successful in that a river of white can be discerned running vertically through most of the red region. In addition, at the very centre of the figure, there is a white patch reflecting the finite smallest value $J_r = 0.0002\,\mathrm{kpc}^2\,\mathrm{Myr}$ adopted: TM has difficulty computing tori for very small actions. This hole could be filled with tori computed with the epicycle approximation, which is at its most precise in this region.

It is worth noting that the difficulty sampling the UV plane at small $|U|$ is directly related to the fact that the real-space density generated by an orbit always diverges near its boundaries, and by Liouville's theorem, its velocity-space density has to be low there. Put another way, the velocity-space density along $U = v_{R\odot}$ is inevitably contributed by a small number of stars that each contribute a large probability density at $U = v_{R\odot}$.

In Fig. 13, another blemish is evident at about four o'clock: a wedge that is clear of red dots. The bulk of the red points are computed using non-resonant perturbation theory, while the points that bound the region of trapped orbits are computed with resonant perturbation theory – red points are contributed by circulating orbits and black/blue points by librating orbits. Since resonant and non-resonant perturbation theories involve different approximations, their results do not match perfectly across the join (cf. Figs 10 and 12). In particular, at the left-hand edge of the red crescent, similar velocities are obtained with different values of J_ϕ, and when this happens, the figure is redder than usual. At the right-hand edge of the crescent, this overpopulation is compensated by a small empty region. This blemish might be smoothed by shifting the transfer to non-resonant theory further from the region of entrapment.

Each point in Fig. 13 is associated with a value of J_r and a value of either J_ϕ (if circulating) or $\mathcal{J}$ (if librating). Fig. 15 shows the curves (magenta for J_r, broken blue for J_ϕ, black for $\mathcal{J}$) on which these integrals are constant. All points share the same value $J_z = 0.0025\,\mathrm{kpc}^2\,\mathrm{km\,s}^{-1}$. In the absence of the bar's contribution to the potential Φ_2, we would have $J_\phi = R_0(v_{\phi\odot} + V)$ so contours of constant J_ϕ would be straight horizontal lines. Φ_2 modifies J_ϕ such that its contours (broken blue) cease to be horizontal and straight. In the region of trapping by CR, J_r (magenta) is complemented by $\mathcal{J}$, the action of libration, whose (grey) contours form asymmetric arches.

6.3 Orbits trapped at the OLR

The upper panel of Fig. 15 is for pattern speed $\omega_{\mathrm{p}} = 0.038\,\mathrm{Myr}^{-1}$, while the lower panel is for $\omega_{\mathrm{p}} = 0.040\,\mathrm{Myr}^{-1}$. Comparison of these panels reveals how sensitive local velocity space is to the pattern speed. This sensitivity is a consequence of how close the Sun is to the edge at $R \sim R_{\mathrm{edge}}$ of the region of entrapment by corotation: when ω_{p} is lowered this edge shifts outwards and displacement by a distance that is small compared to R_0 is not small compared to $R_0 - R_{\mathrm{edge}}$.

At the top of Fig. 13, the curves of constant J_r terminate where they encounter the region of entrapment by the OLR. Fig. 16 is the corresponding plot for the faster pattern speed $\omega_{\mathrm{p}} = 0.040\,\mathrm{Myr}^{-1}$. The regions within which orbits are trapped have both moved down,

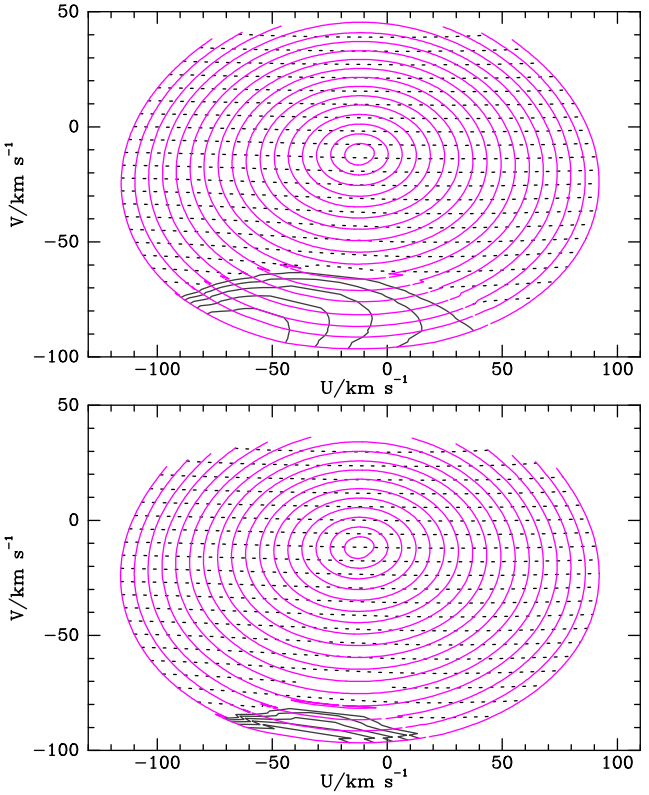

Figure 15. Contours in the UV plane on of constant integrals of motion. J_r is constant on the magenta curves, while generalized angular momentum, J_ϕ, is constant on the dotted curves. The full grey curves are contours of constant action of libration around CR, $\mathcal{J}$. The upper panel is for $\omega_\mathrm{p} = 0.038\,\mathrm{Myr}^{-1}$, while the lower panel is for $\omega_\mathrm{p} = 0.040\,\mathrm{Myr}^{-1}$.

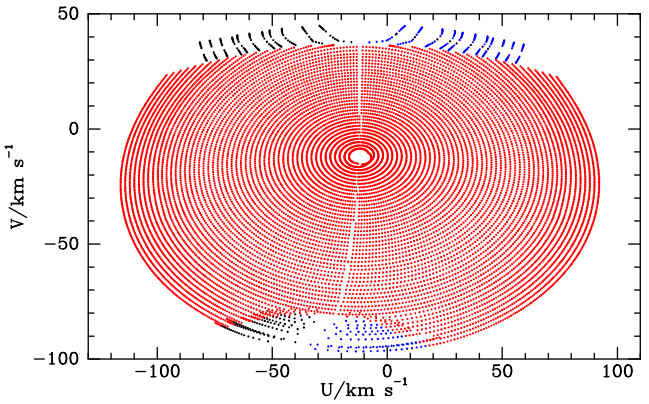

Figure 16. As Fig. 13 but for pattern speed $\omega_\mathrm{p} = 0.040\,\mathrm{Myr}^{-1}$ and with the velocities of orbits trapped at the OLR appearing as 'hair' on top.

so the region within which orbits are trapped at OLR is now clearly visible at the top of the figure. The black dots generated by orbits trapped by the OLR line up along curves of constant $J_3' = J_\phi - 2J_r$, which have both left and right branches. Each orbit appears at four points along the curve associated with its value of J_3'. Orbits with large values of the libration action $\mathcal{J}$ appear towards the top and bottom ends of each stubby line of dots, while orbits with small values of $\mathcal{J}$ appear either side of the middles of these lines. Hence, contours of constant $\mathcal{J}$ delineate a highly elongated and slightly

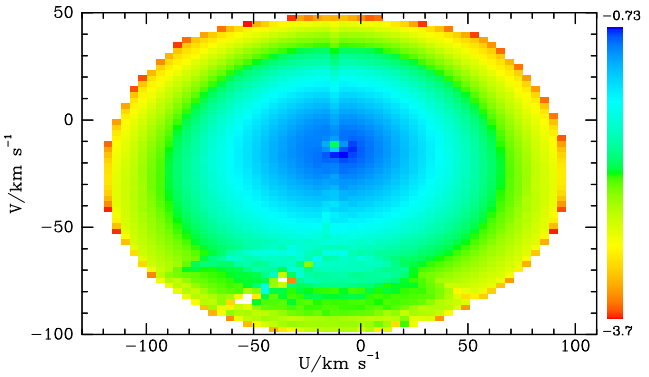

Figure 17. A possible density of stars in the UV plane at the Sun-like location $(R, z, \phi) = (8\,\mathrm{kpc}, 10\,\mathrm{pc}, 155^\circ)$. In the region of circulation, the density is given by the DF of Piffl et al. (2014). In the region of entrapment, the density is computed from the same DF, but using the actions of the perfectly resonant, axisymmetric orbit regardless of the action of libration around this orbit. The pattern speed is $\omega_\mathrm{p} = 0.038\,\mathrm{Myr}^{-1}$.

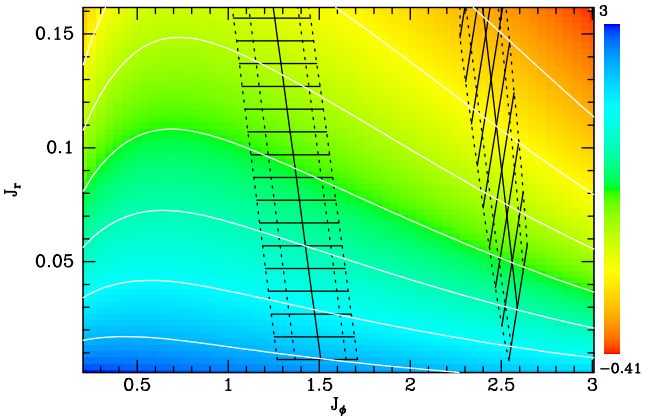

Figure 18. The colours and white contours indicate on a log scale the value of the DF for the adopted axisymmetric Galaxy model. The regions within which orbits are trapped by the bar with $\omega_\mathrm{p} = 0.038\,\mathrm{Myr}^{-1}$ at either corotation or the OLR are marked by ladders as in Fig. 4.

curved island. The OLR region in Fig. 16 contains eleven black and eleven blue lines, and each pair of lines corresponds to the outermost eleven red ellipses, being the ellipses with the largest values of J_r.

Fig. 17 shows the density of stars in the UV plane that is predicted by a plausible DF $f(\boldsymbol{J})$. Colours indicate logarithms to base 10 of the density. We base our DF on the work of Piffl et al. (2014), who fitted a DF to data from the Sloan Digital Sky Survey (Jurić et al. 2008, SDSS) and the Radial Velocity Experiment (RAVE; Steinmetz et al. 2006). Their DF is based on the assumption that the Galaxy is axisymmetric and has to be adapted to encompass non-axisymmetry. The colours and contours in Fig. 18 show the value of the DF in the same slice $J_z = 0.0025\,\mathrm{kpc}^2\,\mathrm{Myr}^{-1}$ through action space for which Fig. 4 shows values of H_0. The value of the DF diminishes rapidly with increasing J_r and more gradually with increasing J_ϕ. Since stars trapped at corotation oscillate along the rungs of the figure's left-hand ladder, they move between regions of high f on the left and low f on the right. By Jeans' theorem the value of the true DF f_true must be a function of the constants of motion. Consequently, in the region of trapping we must replace J_ϕ in the argument list of f_true by $\mathcal{J}$, the libration action, which controls how far

each side of the line of exact resonance a star moves as it librates. In particular, at a given value of J_r, $f_{\rm true}$ must take the same value just to the right of the dashed line that marks the left-hand boundary of the trapping region, as it does just to the left of the dashed line that forms the right-hand boundary of the trapping region. In fact, the simplest possible structure for $f_{\rm true}$ is that it is constant along each of the rungs of the ladder that marks the trapping region in Figs 4 and 18. Monari et al. (2017) adopted this ansatz. The actual population will be determined by the precise history of bar formation and lies beyond the scope of this paper. It is, however, a question that can be addressed by an extension of the modelling technique of Aumer, Binney & Schönrich (2016).

In the region populated by circulating orbits, we simply evaluate the Piffl et al. (2014) DF on the given numbers (J_r, J_z, J_ϕ). In the region populated by trapped orbits, we evaluate the Piffl et al. DF using the actions of the perfectly resonant orbit from which it is obtained by adding some amplitude of libration. This choice leaves the star density in the region of entrapment higher than at points outside this region that are similar distances from the centre of the figure. However, within the trapped zone one can in principle take the DF to be *any* non-negative function of the integrals $(J_r, J_z, \mathcal{J})$.

The observed distribution of local stars in the UV plane shows an overdensity centred on $\sim(-35, -50)\,{\rm km\,s^{-1}}$ that is called the Hercules Stream. Dehnen (1999) suggested that it is caused by stars being trapped by the bar's OLR, and by modelling this process derived $\omega_{\rm p} = 54\,{\rm km\,s^{-1}\,kpc^{-1}}$. As was noted in Section 2.1, there is now strong evidence that the bar's pattern speed is not greater than $\omega_{\rm p} = 40\,{\rm km\,s^{-1}}$, with the consequence that the OLR lies well outside R_0 and could only affect local velocity space at positive values of V. With the lower pattern speed, we instead lie not far outside the bar's CR, and Pérez-Villegas et al. (2017) have shown that the model of the bar developed by Wegg et al. (2015) with $\omega_{\rm p} = 39\,{\rm km\,s^{-1}\,kpc^{-1}}$ predicts a feature rather like the Hercules stream that is caused by stars trapped into libration around the Lagrange point L_4. Fig. 17 shows that in our model of the bar stars trapped at corotation appear at significantly smaller values of V: the region of entrapment does not extend above $V = -62\,{\rm km\,s^{-1}}$. On the other hand, it is centred on $U \sim -30\,{\rm km\,s^{-1}}$, rather as in the observations.

The region of entrapment can be moved further up by lowering $\omega_{\rm p}$, or by adopting a locally rising circular-speed curve.

7 DISCUSSION

7.1 Relation to previous work

We have addressed much the same problem as Monari et al. (2016) and Monari et al. (2017) from a rather different perspective. Monari et al. (2016) use angle-action variables to compute the first-order change f_1 in an unperturbed DF $f_0(\boldsymbol{J})$ when a non-axisymmetric component is added to the potential. As a resonance is approached, f_1 diverges, so there is a band in action space around a resonant torus within which $f_0 + f_1$ is not non-negative and hence is manifestly in error. They show that this problem is not mitigated by going to second order. Monari et al. (2017) use the standard pendulum equation to determine the width of the trapping region, but they do not compute actions for trapped orbits, and whenever $|f_1| > f_0$ they use

$$f = \begin{cases} 2f_0 & \text{if } f_1 > 0, \\ 0 & \text{otherwise.} \end{cases} \tag{56}$$

Using this prescription and the angle-action coordinates provided by the epicycle approximation, Monari et al. (2017) compute the structure of the UV plane for a variety of pattern speeds and bar strengths. The main differences with our work are (a) we use tori rather than the epicycle approximation so we retain accuracy even for eccentric orbits, (b) we are not restricted to planar orbits and (c) we have complete control of the DF of trapped orbits, so our DF is finite but discontinuous at the edges of the trapping region as it should be. The practicalities of the two calculations differ significantly because tori provide the transformation $(\boldsymbol{\theta}, \boldsymbol{J}) \rightarrow (\boldsymbol{x}, \boldsymbol{v})$, while the epicycle approximation provides the inverse transformation $(\boldsymbol{x}, \boldsymbol{v}) \rightarrow (\boldsymbol{\theta}, \boldsymbol{J})$. The latter is in many ways the more convenient direction, and by using the Stäckel fudge (Binney 2012a) for an axisymmetric system one can proceed in this direction without losing accuracy for eccentric orbits. However, the Stäckel fudge is not applicable to rotating non-axisymmetric potentials and it does not tackle resonant trapping, so currently the impact of resonant trapping can only be reliably computed using tori.

Although resonant trapping changes individual orbits qualitatively, Fig. 17 demonstrates that the impact of trapping on velocity space *may* be quite modest, depending on the form that the DF takes in the region of entrapment. This conclusion probably explains why axisymmetric models such as that of Piffl et al. (2014) have yielded excellent fits to data.

7.2 Poisson noise and modelling strategy

The main difficulty encountered when using tori is getting the sampling density right. For example, in a plot of the UV plane one wants a dense sampling near the peak of the star distribution, that is near the local standard of rest. Here, U, V and so on are small and small changes in U, V, W correspond to tiny changes in $J_r \propto U^2$ and $J_z \propto W^2$. Hence, tori must be constructed on a very non-uniform grid in action space. It is similarly necessary to sample densely in J_ϕ near the values for which a star reaches apocentre or pericentre at the location for which the UV plane is required. Fortunately, torus interpolation makes dense sampling in a particular region computationally affordable, and Fig. 17 demonstrates that the non-uniform action-spaced grid of Fig. 14 provides adequate sampling of circulating orbits. The sampling of resonantly trapped orbits needs refinement, however.

Custom sampling of action space can be avoided by devising an algorithm that interpolates to a general point in velocity space the values taken on a suboptimal grid by the constants of motion, (J_r, J_z, J_ϕ) or $(J_r, J_z, \mathcal{J})$ as appropriate. An algorithm of this type was used to plot the contours of Fig. 15, and a similar algorithm lies at the heart of the chemodynamical evolution code that underpins Schönrich & McMillan (2017). This procedure seems to be the most promising way forward for chemodynamical modellers.

Poisson noise is a constant irritant when one seeks to model galaxies with precision, so it is a major headache when modelling the Milky Way. Indeed, to extract a reasonable plot of the local UV plane from the M2M model of Wegg et al. (2015), Pérez-Villegas et al. (2017) had to upgrade the model significantly because the solar neighbourhood contains only a very small fraction of the Galaxy's stars. Plots such as Fig. 17 show that the combination of $f(\boldsymbol{J})$ modelling and torus interpolation enables one to beat Poisson noise down to low levels at small computational cost: even with the current not-optimized version of TM this figure can be computed from scratch in of order half a processor-hour. The UV plane predicted by a different DF can be computed in less than a second.

In standard Schwarzschild modelling, one starts from a potential $\Phi(\boldsymbol{x})$ and seeks orbit weights that are consistent with Φ and observational constraints. Unless the system is extremely simple, it is not unlikely that Φ cannot be generated by any set of non-negative weights. When tori are employed, one can start with Φ and adjust the weights of tori (or the parameters of DFs for each component) until reasonable agreement with data are achieved. Then one can relax the potential to exact self-consistency (Binney 2014; Piffl, Penoyre & Binney 2015) to obtain a completely sound model. Standard Schwarzschild modelling does not permit this step to self-consistency.

In summary, there are many reasons why classical Schwarzschild modelling, in which orbits are used as time sequences, is abandoned in favour of torus modelling: tori are simply more compact and very much more powerful than classical orbits. In point of historical fact, Martin Schwarzschild himself took the first step towards torus modelling (Ratcliff, Chang & Schwarzschild 1984).

7.3 Accuracy and chaos

The quality of the fits delivered by perturbation theory is remarkable. For example, the length of black ladder rungs in Fig. 4 and the qualitative difference between the full black and broken blue invariant curves in Fig. 7 show that along an orbit trapped by the OLR the angular momentum and radial action typically make large excursions and trapped orbits do not keep close to the perfectly resonant torus that provides the numbers used to construct a whole family of trapped and even circulating orbits. Yet surfaces of section and plots in real space demonstrate that orbits can be accurately reconstructed perturbatively. On account of a poor initial choice of the bar strength, most of the figures presented have been plotted for a bar that is almost twice as strong. The quality of fits in those figures is not much inferior to that shown here. Thus, the Galaxy does not require us to push perturbation theory near its limits. It is remarkable that such impressive results can be obtained by averaging to zero the non-resonant terms in the Fourier expansion of the Hamiltonian. The legitimacy of this procedure is by no means self-evident.

The extent to which the dynamics of disc stars is independent of J_z is striking. In particular, stars from the thin and thick discs that have similar values of J_r and J_ϕ will respond to the bar in essentially identical ways.

Another remarkable feature of this study is the absence of any sign of chaos. It is very likely that this absence reflects the pure $m = 2$ nature of the applied non-axisymmetry. A natural next step is to add a smaller $m = 4$ component, see what additional resonances emerge, and understand if/how these give rise to some chaotic regions. Numerical integrations of chaotic orbits suggest that they are piece-wise quasi-periodic, so they can be understood as orbits that move between tori belonging to different resonantly trapped families. The prospect of bringing order into chaos by representing orbits as superpositions of tori is an exciting one.

7.4 Spiral structure

The technique explored here in the context of the bar is equally applicable to a steady spiral perturbation. Whether the assumption of a constant pattern speed is at all useful in the context of spiral structure remains to be seen, however. Since the gravitational field of a tightly wound spiral pattern decays more rapidly with $|z|$ than that of a bar, one would expect the Fourier decomposition of a spiral arm to have more power in terms with non-vanishing k_z than the bar provides. Consequently, contrary to what we have found in the case of the bar, we expect significant differences between the responses of thin- and thick-disc stars to a spiral. Moreover, if a spiral pattern can bring J_z into play, it will lead to more interesting dynamics than we have encountered from the bar. Finally, realistic spiral patterns will have significant power in more than one azimuthal quantum number, and thus raise the prospect of cross-talk between resonances. Exploring these issues will require significant effort.

7.5 Connection to gyrokinetics

Figs 8 and 10 are strongly reminiscent of the gyrokinetic theory of a magnetized plasma. In that theory, one computes the dynamics of the points around which electrons rapidly gyrate with an adiabatically conserved magnetic moment. Near CR, there are two adiabatically conserved quantities, J_r and J_z. Moreover Fig. 9 indicates that although a star's angular momentum changes significantly along an orbit trapped by CR, it is a unique function of the location of the gyrocentre, i.e. θ_ϕ. This is precisely the prediction of perturbation theory to the extent that it is possible to neglect the non-resonant terms: the angular momentum is $J_\phi = J_{\phi\,\mathrm{res}} + \Delta(\theta_\phi)$. To a good approximation dynamics, near corotation can be reduced to the one-dimensional motion of quasi-particles that are endowed with specified quantities of radial and vertical action.

8 CONCLUSIONS

Ours is a barred Galaxy, so work with axisymmetric Galaxy models is inherently limited. In fact, it is in many ways surprising what good fits one can obtain with axisymmetric models to data for stars in the extended solar neighbourhood (Binney et al. 2014). As the available data become richer and more precise, we cannot avoid progressing to employing non-axisymmetric models for the interpretation of astrometric data.

The impact of non-axisymmetric components of the potential is typically localized to the regions of phase space in which a resonant condition is nearly satisfied. A key but easily overlooked point here is that orbital tori are required even to identify these regions – the concept of resonance is inextricably tied up with that of angle-action coordinates and thus with orbital tori. Given an axisymmetric gravitational potential, TM can be used to construct a system of angle-action coordinates for a very closely related Hamiltonian $H_0(\boldsymbol{J})$. Any difference between $H_0(\boldsymbol{J})$ and the true Hamiltonian is liable to have a significant impact on orbits in a region of phase space within which a resonant condition is nearly satisfied. In particular, there is often a region within which orbits are trapped by the resonance. Trapped orbits are qualitatively different from their nearby untrapped brethren.

B16 investigated trapping of the orbits of halo stars by the resonance $\Omega_r \simeq \Omega_z$ in an axisymmetric potential. Perturbation theory was used to construct orbital tori that allow accurate reconstructions of trapped orbits. Here, we have extended this work to the construction of tori that provide accurate representations of orbits that are strongly affected by resonances with the Galactic bar.

In the case of the bar, perturbative effects on tori need to be considered not only in the case of trapping but also when an orbit circulates outside the trapping region, because TM's fitting routine ignores all non-axisymmetric components of the potential, and in contrast to the situation encountered in B16, its tori do not provide adequate fits to all circulating orbits.

We have used resonant perturbation theory to construct orbital tori for a realistic representation of our barred Galaxy. The

constructed tori provide accurate representations of numerically integrated orbits because (a) they employ the sophisticated pendulum equation introduced by Kaasalainen (1994) rather than the standard pendulum equation, and (b) we employ the angle-action coordinates provided by TM rather than the epicycle approximation.

Having orbital tori rather than just numerically integrated orbits is valuable for several reasons. First, orbital tori provide an extremely compact representation of orbits: several dozen numbers encode everything you could possible wish to compute about the infinite number of orbits that can be constructed by interpolating between tori. Moreover, tori are quantified by actions, which are adiabatically invariant constants of motion that also allow one to compute the phase-space volumes occupied by sets of orbits. Other substantial advantages of using tori are the ability to use an analytic DF to populate orbits in a considered manner, and the ability to determine whether a given orbit will ever reach a particular location, such as the immediate solar neighbourhood, and if so with what velocities. Finally, tori make it possible to relax the potential in which a multicomponent system is constructed to self-consistency.

We have illustrated this power of orbital tori by using them to construct a slice through velocity space at the Sun. To minimize the impact of Poisson noise in this slice, action space had to be sampled in a non-uniform manner because in some parts of velocity space the stellar density derives from a small number of orbits that contribute with large weights. This generic drawback of orbit modelling can be side-stepped by building a map of the value of each action in velocity space from the value it takes on an irregular distribution of points contributed by individual tori.

ACKNOWLEDGEMENTS

I thanks the referee Martin Weinberg for insightful comments. This work was supported by the European Research Council under the European Union's Seventh Framework Programme (FP7/2007-2013)/ERC grant agreement no. 321067.

REFERENCES

Antoja T., Figueras F., Romero-Gómez M., Pichardo B., Valenzuela O., Moreno E., 2011, MNRAS, 418, 1423
Arnold V., 1989, Mathematical Methods of Classical Mechanics, Vol. 60. Springer, New York
Aumer M., Binney J., Schönrich R., 2016, MNRAS, 459, 3326
Binney J., 2012a, MNRAS, 426, 1324
Binney J., 2012b, MNRAS, 426, 1328
Binney J., 2014, MNRAS, 440, 787
Binney J., 2016, MNRAS, 462, 2792 (B16)
Binney J., McMillan P. J., 2016, MNRAS, 456, 1982
Binney J., Piffl T., 2015, MNRAS, 454, 3653
Binney J., Spergel D., 1982, ApJ, 252, 308
Binney J., Spergel D., 1984, MNRAS, 206, 159
Binney J., Tremaine S., 2008, Galactic Dynamics, 2nd edn. Princeton Univ. Press, Princeton, NJ
Binney J., Gerhard O. E., Stark A. A., Bally J., Uchida K. I., 1991, MNRAS, 252, 210
Binney J. et al, 2014, MNRAS, 439, 1231
Blitz L., Spergel D. N., 1991, ApJ, 379, 631
Bovy J., Rix H.-W., 2013, ApJ, 779, 115
Chirikov B. V., 1979, Phys. Rep., 52, 263
de Lorenzi F., Debattista V. P., Gerhard O., Sambhus N., 2007, MNRAS, 376, 71
De Simone R., Wu X., Tremaine S., 2004, MNRAS, 350, 627
Dehnen W., 1998, AJ, 115, 2384
Dehnen W., 1999, ApJ, 524, L35
Dehnen W., 2009, MNRAS, 395, 1079
Dehnen W., Binney J., 1998, MNRAS, 294, 429
Deng L.-C. et al., 2012, Res. Astron. Astrophys., 12, 735
Hahn C. H., Sellwood J. A., Pryor C., 2011, MNRAS, 418, 2459
Jeans J. H., 1915, MNRAS, 76, 70
Jurić M. et al., 2008, ApJ, 673, 864
Kaasalainen M., 1994, MNRAS, 268, 1041
Lépine J. R. D., Roman-Lopes A., Abraham Z., Junqueira T. C., Mishurov Y. N., 2011, MNRAS, 414, 1607
Long R. J., Mao S., 2010, MNRAS, 405, 301
McMillan P. J., 2011, MNRAS, 414, 2446
McMillan P. J., 2013, MNRAS, 430, 3276
Monari G., Famaey B., Siebert A., 2016, MNRAS, 457, 2569
Monari G., Famaey B., Fouvry J.-B., Binney J., 2017, MNRAS, 471, 4314
Monari G., Famaey B., Siebert A., Duchateau A., Lorscheider T., Bienaymé O., 2017, MNRAS, 465, 1443
Morganti L., Gerhard O., 2012, MNRAS, 422, 1571
Pérez-Villegas A., Portail M., Wegg C., Gerhard O., 2017, ApJ, 840, L2
Piffl T. et al., 2014, MNRAS, 445, 3133
Piffl T., Penoyre Z., Binney J., 2015, MNRAS, 451, 639
Ratcliff S. J., Chang K. M., Schwarzschild M., 1984, ApJ, 279, 610
Sanders J. L., Binney J., 2015, MNRAS, 447, 2479
Schönrich R., McMillan P., 2017, MNRAS, 467, 1154
Schönrich R., Binney J., Dehnen W., 2010, MNRAS, 403, 1829
Schwarzschild M., 1979, ApJ, 232, 236
Sellwood J. A., 2010, MNRAS, 409, 145
Sormani M. C., Binney J., Magorrian J., 2015, MNRAS, 454, 1818
Steinmetz M. et al., 2006, AJ, 132, 1645
Syer D., Tremaine S., 1996, MNRAS, 282, 223
Wang Q., Wang Y., Liu C., Mao S., Long R. J., 2017, MNRAS, 470, 2949
Wegg C., Gerhard O., Portail M., 2015, MNRAS, 450, 4050

APPENDIX A: NEW CLASSES FOR TM

To implement the algorithms presented here, four new classes, `eTorus`, `iTorus`, `resTorus_c` and `resTorus_L`, have been introduced to the TM (Binney & McMillan 2016). Objects of type `eTorus` are just tools to be exploited by objects in the other three classes. Whereas an object of class `iTorus` uses non-resonant perturbation theory so provide non-axisymmetric tori away from resonances, objects of the last two classes use resonant perturbation theory and provide tori near resonances.

A1 Class eTorus

An `eTorus` comprises an axisymmetric `Torus` together with the ten largest Fourier coefficiets h_k of the full Hamiltonian on that torus. The principal methods in this class are listed in Table A1.

A2 Class iTorus

An `iTorus` is an object whose methods encode non-resonant perturbation theory (Table A2). It is characterized by actions J_i that quantify generalizations of the standard actions of axisymmetric orbits, and it employs a grid of `eTori` to compute its properties. `FullMap` returns the phase-space location given angle values. `containsPoint` returns the number of distinct velocities (if any) at which the torus visits a given spatial location, along with the corresponding values of the angles and the Jacobian $\partial(\boldsymbol{x})/\partial(\boldsymbol{\theta})$. The Boolean `InOrbit` simply determines whether a given point is visited. For given J_r and J_z `get_crit_Jp` returns the values of J_ϕ at which an orbit has apocentre or pericentre at a given location. `SOS` produces an (R, p_R) surface of section.

Table A1. Public methods of an `eTorus`.

`eTorus()`	Null constructor
`eTorus(Actions,Potential*,bar_pot*,double,double)`	Constructs an `eTorus` for given actions and potential. The last two arguments are the pattern speed and the tolerance parameter `tolJ`
`eTorus(Torus&,Potential*,bar_pot*,double)`	Upgrades a `Torus` to an `eTorus`. the last argument is the pattern speed
`AutoFit(Actions,Potential*,bar_pot*,double,double`	Changes an already existing `eTorus` so it has given actions.
`reset(Torus&,Potential*,bar_pot*)`	Changes the home `Torus` and on it computes the $h_{\boldsymbol{k}}$
`Frequencies()`	Returns frequencies
`actions()`	Returns actions
`hn()`	Returns the values of the Fourier coefficients $h_{\boldsymbol{k}}$
`i1(), j1(), k1()`	Return the integer coefficient of θ_r, θ_z and θ_ϕ associated with each term in $h_{\boldsymbol{k}}$
`FullMap(Angles)`	Returns $(R, z, \phi, v_R, v_z, v_\phi)$ of phase-space point referenced by the given angles
`containsPoint(Position&,Velocity&,Velocity&, double&,Angles,Angles&&Velocity&, Velocity&,double&,Angles&,Angles&)`	Places in the Angles arguments the angles at which the torus reaches the given Position. The Velocity and double arguments are returned with the velocities and inverse densities of the visits.
`write_ebf(string,string)`	Writes the `eTorus` to the ebf file named by the first string with tag given by the second string
`read_ebf(string,string)`	Inverse of the above write method

Table A2. Public methods of an `iTorus`.

`iTorus(Actions,eTorus**,int,int,Actions,Actions`	Creates an `iTorus`with the given actions given a grid of `eTorus`s
`eT1(Actions)`	Returns the `eTorus` with the given actions
`hn(), i1(), j1(), k1()`	Return properties of the home `eTorus`
`actions(), omega()`	Return actions and frequencies of home `eTorus`
`FullMap(Angles)`	Returns $(R, z, \phi, v_R, v_z, v_\phi)$ pointed to by given angle
`SOS(ostream&,int)`	Sends surface of section to output stream
`containsPoint(Position&,Velocity*,Angles*, double*,int)`	Returns number of angles (up to maximum specified by last argument) at which Position is visited and leaves angles, velocities and inverse densities of visits in arguments

Here is the code that created the 20 × 30 grid of eTori used to produce figures that required untrapped orbits. Notice that the grid is uniform in $\sqrt{J_r}$ rather than in J_r. `Phi` and and `bar` are pointers to an axisymmetric potential and an $m = 2$ perturbation, respectively.

```
  int nr=30,np=20;
  Actions J,Jgrid,dJ;
  dJ[0]=(sqrt(Jrmax)-sqrt(Jrmin))/(double)
(nr-1);
  dJ[1]=0; dJ[2]=(Jpmax-Jpmin)/(double)
(np-1);
  Jgrid[0]=sqrt(Jrmin)+.5*dJ[0];
  Jgrid[1]=J[1];
  Jgrid[2]=Jpmin+.5*dJ[2];
  eTorus **Tgrid=PJM::matrix<eTorus>(np,nr);
  strcat(fname,"nores.ebf"); bool
writeit=true;
  if(writeit){
   ebf::Write(fname,"/dJ",&dJ[0],"w","",1);
   printf("Computing eTorus grid:\n");
   for(int i=0;i<np;i++){
   J[2]=Jpmin+i*dJ[2];
   for(int j=0;j<nr;j++){
   J[0]=pow(sqrt(Jrmin)+j*dJ[0],2);
   Tgrid[i][j].AutoFit(J,Phi,bar,Omp,tolJ);
   char lab[7];
   sprintf(lab,"eT%d-%d",i,j);
   const string tname(lab);
   Tgrid[i][j].write_ebf(fname,tname);
    }
   }
  } else{
   ebf::Read(fname,"/dJ",&dJ[0],1);
   printf("Reading eTorus grid:\n");
   for(int i=0;i<np;i++){
   for(int j=0;j<nr;j++){
   char lab[7];sprintf(lab,"eT%d-%d",i,j);
   string tname(lab);
   Tgrid[i][j].read_ebf(fname,tname);
    }
   }
  }
  Now
  iTorus T(J,Tgrid,np,nr,Jgrid,dJ);
```

will create an untrapped torus with actions `J`, which can be examined with `T.FullMap`, `T.containsPoint` , etc.

A3 Class resTorus_c

Objects in this class use resonant perturbation theory to compute tori that are trapped, or nearly trapped, at corotation. The principal methods are listed in Table A3. The constructor requires values of J_r, J_z and a rough estimate of the value of J_ϕ for corotation resonance with the given (J_r, J_z) – the estimate of J_ϕ is changed to achieve precise corotation resonance. An `eTorus` with these actions is constructed and the parameters of the pendulum equation found by Taylor expanding the Hamiltonian's Fourier amplitudes around

Table A3. Public methods of an `resTorus_c`.

`resTorus_c(Torus**,int,Actions,Potential*, bar_pot*,double,double)`	Constructor given actions and a pointer to an empty $2 \times n$ grid of tori. The second argument specifies n.
`setI(double)`	Sets variable I that controls the amplitude of libration
`setI(double,int)`	As `setI(double)` but if $I < I_{\rm bot}$, circulates inside corotation if integer is -1
`librationAction()`	Returns action of libration
`librationOmega()`	Returns libration frequency
`from_librationAngle(double,double&,double&)`	Return θ_ϕ, $\mathrm{d}\theta_\phi/\mathrm{d}\theta_{\rm la}$ and offset of J_r from perfectly resonant value
`FullMap(Angles)`	Returns $(R, z, \phi, v_R, v_z, v_\phi)$ for given angles
`SOS(ostream&,int)`	Send $\phi = \pi/2$ surface of section to ostream
`containsPoint(Position&,Velocity*,Angles*, Angles*,double*)`	Returns number of angles at which Position is visited and leaves angles, velocities and inverse densities of visits in arguments
`getJs(Actions&,Actions&,double)`	Returns extremes of unperturbed actions on orbit
`get_resJp()`	Returns actions of underlying perfectly resonant torus
`omega()`	Returns frequencies

the values taken on the perfectly resonant `eTorus`. From these parameters, the extent of the region of entrapment is determined and then a grid of tori is computed so any trapped or nearly trapped torus can be constructed by interpolation.

A particular trapped torus is specified by giving a value of the variable I with `setI`. Given an instance `resTorus_c T`, the maximum permitted value, `T.Imax`, generates the torus with no libration, while the value `T.Imin` generates the torus with maximum libration. Values smaller than `T.Imin` generate circulation. By default circulation takes place outside corotation, but `T.setI(1.05*T.Imin,-1)` will generate circulation inside corotation.

With `Phi` a pointer to an axisymmetric potential and `bar` a pointer to an $m = 2$ perturbation, the following code will generate data for Fig. 10.

```
FILE *ofile; ofile=fopen("corot.out",
"w"); Actions J; J[0]=.1;
J[1]=0.0025; J[2]=2; int np=5;
double Omp=0.04,tolJ=0.003; Torus **Tgrid;
Tgrid = PJM::matrix<Torus>(2,np);
resTorus_c T(Tgrid,np,J,Phi,bar,Omp,tolJ);
T.setI(1.1*T.Imin,1); J=T.get_resJp();
Angles A; Frequencies Omres=T.omega();
int NS=5000; double x[NS],y[NS];
double Jl=T.librationAction(); dou-
ble dt=10*PI/fabs(Omres[2])/(double)NS;
fprintf(ofile,"%f %f %f\n",(NS-
1)*dt,J[0],Jl); for(int i=0;i<NS;i++){
double t=i*dt; A[0]=Omres[0]*t;
A[1]=Omres[1]*t; A[2]=Omres[2]*t; GCY
gcy=T.FullMap(A); x[i]=gcy[0]*cos(gcy[2]);
y[i]=gcy[0]*sin(gcy[2]); for(int
j=0;j<6;j++){
fprintf(ofile,"%f ",gcy[j]);
}
fprintf(ofile,"\n"); }
```

Connecting the points (x, y) stored in `x[],y[]` will now produce the red curve in Fig. 10, while an orbit integration can be launched from any of the phase-space points written to 'corot.out'.

A4 Class resTorus_L

Instances of this class generate tori that are trapped or nearly trapped at a Lindblad resonance. The layout is very similar to that of `resTorus_c` (Table A4). One more argument is required, namely the integer 3-vector `resN`, which is (1, 0, 2) for OLR and (1, 0, −2) for ILR. The following statements create a torus with the values of J_r and J_z given in `J` that is trapped at OLR.

```
int nr=5; Tgrid = PJM::matrix<Torus>(nr,2);
int sc[3]={1,0,2}; int3 resN(sc); resTorus_L
T(Tgrid,nr,J,Phi,bar,Omp,resN,tolJ);
T.setI(.8*T.Imin());
```

Table A4. Public methods of an `resTorus_L`.

`resTorus_L(Torus**,int,Actions,Potential*, bar_pot*,double,int3,double)`	Constructor given actions and a pointer to an empty $2 \times n$ grid of tori. The second argument specifies n.
`setI(double)`	Sets variable I that controls the amplitude of libration
`setI(double,int)`	As `setI(double)` but if $I < I_{\rm bot}$, circulates inside corotation if integer is -1
`librationAction()`	Returns action of libration.
`librationOmega()`	Returns libration frequency
`from_librationAngle(double,double&,double&)`	Return θ_1', $\mathrm{d}\theta_1'/\mathrm{d}\theta_{\rm la}$ and offset in J_1' from the perfectly resonant value
`FullMap(Angles)`	Returns $(R, z, \phi, v_R, v_z, v_\phi)$ for given angles
`SOS(ostream&,int)`	Send $\phi = \pi/2$ surface of section to ostream
`containsPoint(Position&,Velocity*,Angles*, Angles*,double*)`	Returns number of angles at which Position is visited and leaves angles, velocities and inverse densities of visits in arguments
`getJs(Actions&,Actions&,double)`	Returns extremes of unperturbed actions on orbit
`get_resJp()`	Returns actions of perfectly resonant `eTorus`
`omega()`	Returns frequencies
`prime_it(Action,bool)`	If the `bool`=1, $J' \to J$, else reverse

The properties of this torus can then be explored with `T.FullMap`, `T.containsPoint`, etc., exactly as for any other torus.

A5 Calling programs

To illustrate the use of these tools the TM depository contains three main programs: `corot.cc`, `lindblad.cc` and `nores.cc`. The first two programs will

(i) compute the edges of the ladders plotted in Figs 4 and 18;
(ii) compute the velocities at which a resonantly trapped torus visits a Sun-like location;
(iii) plot a trapped or near-trapped orbit and produce the data required for a surface of section.

The third main program reads files created by the first two and computes the velocities at which non-resonant orbits reach a Sun-like location. It will also produce data to plot such an orbit.

APPENDIX B: FINDING VELOCITIES AT A GIVEN LOCATION

Whereas it is trivial to reach a given azimuth ϕ_0 on an axisymmetric torus (by adding whatever we like to θ_ϕ), on a non-axisymmetric torus θ_ϕ becomes a non-trivial variable in the sense that we cannot change it without changing the toy angles $\boldsymbol{\theta}^{\rm T}$, so the quantity to be minimized by `containsPoint` must have three terms

$$\chi^2 = (R - R_0)^2 + (z - z_0)^2 + R_0^2(\phi - \phi_0)^2 \tag{B1}$$

rather than just the first two. Hence, we now need the derivatives of ϕ with respect to $\boldsymbol{\theta}^{\rm T}$ and $\boldsymbol{J}^{\rm T}$. Since

$$\phi = u + \theta_\phi^{\rm T} - {\rm sgn}(J_\phi^{\rm T})\theta_\vartheta^{\rm T} \tag{B2}$$

with

$$\sin u \equiv \cot i \tan\vartheta \ \text{ and } \ \cos i \equiv \frac{J_\phi^{\rm T}}{J_\vartheta^{\rm T} + |J_\phi^{\rm T}|} \equiv \frac{J_\phi^{\rm T}}{L}, \tag{B3}$$

we obtain

$$\begin{aligned}
\frac{\partial\phi}{\partial\theta_r^{\rm T}} &= \sec u \frac{\cot i}{\cos^2\vartheta}\frac{\partial\vartheta}{\partial\theta_r^{\rm T}}\\
\frac{\partial\phi}{\partial\theta_\vartheta^{\rm T}} &= \sec u \frac{\cot i}{\cos^2\vartheta}\frac{\partial\vartheta}{\partial\theta_\vartheta^{\rm T}} - {\rm sgn}(J_\phi^{\rm T})\\
\frac{\partial\phi}{\partial\theta_\phi^{\rm T}} &= 1.
\end{aligned} \tag{B4}$$

Here, the last equation follows because $\partial\vartheta/\partial\theta_\phi^{\rm T} = 0$ and ϑ is latitude rather than the conventional polar angle because TM adopts this notation. Similarly,

$$\begin{aligned}
\frac{\partial\phi}{\partial J_r^{\rm T}} &= \frac{\partial u}{\partial J_r^{\rm T}} = \sec u \frac{\cot i}{\cos^2\vartheta}\frac{\partial\vartheta}{\partial J_r^{\rm T}}\\
\frac{\partial\phi}{\partial J_\vartheta^{\rm T}} &= \frac{\partial u}{\partial J_\vartheta^{\rm T}} = \sec u \left(\frac{\cot i}{\cos^2\vartheta}\frac{\partial\vartheta}{\partial J_\theta^{\rm T}} - \frac{\cot\vartheta}{\sin^3 i}\frac{J_\phi^{\rm T}}{L^2}\right)\\
\frac{\partial\phi}{\partial J_\phi^{\rm T}} &= \frac{\partial u}{\partial J_\phi^{\rm T}} = \sec u \left(\frac{\cot i}{\cos^2\vartheta}\frac{\partial\vartheta}{\partial J_\phi^{\rm T}} + \frac{\cot\vartheta}{\sin^3 i}\frac{J_\vartheta^{\rm T}}{L^2}\right).
\end{aligned} \tag{B5}$$

TM finds the velocities at which an axisymmetric torus visits a given location $\boldsymbol{x}$ by varying the toy angle variables, which are most directly related to ordinary phase-space coordinates. When the torus is not axisymmetric this is not a good strategy, not least because on a trapped torus many values of $\boldsymbol{\theta}^{\rm T}$ are inaccessible. So `iTorus`, `resTorus_c` and `resTorus_L` all search in true angles.

Let $(\boldsymbol{\theta}', \boldsymbol{J}')$ denote the angle-action coordinates of a non-axisymmetric torus, $(\boldsymbol{\theta}, \boldsymbol{J})$ denote angle-action coordinates for a realistic axisymmetric Galactic potential, and $(\boldsymbol{\theta}^{\rm T}, \boldsymbol{J}^{\rm T})$ denote the 'toy' angle-action coordinates of an isochrone potential. Then $(\boldsymbol{\theta}, \boldsymbol{J})$ and $(\boldsymbol{\theta}^{\rm T}, \boldsymbol{J}^{\rm T})$ are related by TM's standard generating function

$$S(\boldsymbol{\theta}^{\rm T}, \boldsymbol{J}) = \boldsymbol{\theta}^{\rm T}\cdot\boldsymbol{J} + 2\sum_{\boldsymbol{n}} S_{\boldsymbol{n}}(\boldsymbol{J})\sin(\boldsymbol{n}\cdot\boldsymbol{\theta}^{\rm T}). \tag{B6}$$

S and its derivatives are provided by TM. We use the Newton–Raphson algorithm to find the values of $\boldsymbol{\theta}'$ at which the non-axisymmetric torus $\boldsymbol{J}'$ passes through the point $\boldsymbol{x}$. We have

$$\left(\frac{\partial\boldsymbol{x}}{\partial\boldsymbol{\theta}'}\right)_{\boldsymbol{J}'} = \left(\frac{\partial\boldsymbol{x}}{\partial\boldsymbol{\theta}^{\rm T}}\right)_{\boldsymbol{J}^{\rm T}}\left(\frac{\partial\boldsymbol{\theta}^{\rm T}}{\partial\boldsymbol{\theta}'}\right)_{\boldsymbol{J}'} + \left(\frac{\partial\boldsymbol{x}}{\partial\boldsymbol{J}^{\rm T}}\right)_{\boldsymbol{\theta}^{\rm T}}\left(\frac{\partial\boldsymbol{J}^{\rm T}}{\partial\boldsymbol{\theta}'}\right)_{\boldsymbol{J}'} \tag{B7}$$

and

$$\left(\frac{\partial\boldsymbol{J}^{\rm T}}{\partial\boldsymbol{\theta}'}\right)_{\boldsymbol{J}'} = \left(\frac{\partial\boldsymbol{J}^{\rm T}}{\partial\boldsymbol{J}}\right)_{\boldsymbol{\theta}^{\rm T}}\left(\frac{\partial\boldsymbol{J}}{\partial\boldsymbol{\theta}'}\right)_{\boldsymbol{J}'} + \left(\frac{\partial\boldsymbol{J}^{\rm T}}{\partial\boldsymbol{\theta}^{\rm T}}\right)_{\boldsymbol{J}}\left(\frac{\partial\boldsymbol{\theta}^{\rm T}}{\partial\boldsymbol{\theta}'}\right)_{\boldsymbol{J}'} \tag{B8}$$

so

$$\begin{aligned}
\left(\frac{\partial\boldsymbol{x}}{\partial\boldsymbol{\theta}'}\right)_{\boldsymbol{J}'} = &\left\{\left(\frac{\partial\boldsymbol{x}}{\partial\boldsymbol{\theta}^{\rm T}}\right)_{\boldsymbol{J}^{\rm T}} + \left(\frac{\partial\boldsymbol{x}}{\partial\boldsymbol{J}^{\rm T}}\right)_{\boldsymbol{\theta}^{\rm T}}\left(\frac{\partial\boldsymbol{J}^{\rm T}}{\partial\boldsymbol{\theta}^{\rm T}}\right)_{\boldsymbol{J}}\right\}\left(\frac{\partial\boldsymbol{\theta}^{\rm T}}{\partial\boldsymbol{\theta}'}\right)_{\boldsymbol{J}'}\\
&+ \left(\frac{\partial\boldsymbol{x}}{\partial\boldsymbol{J}^{\rm T}}\right)_{\boldsymbol{\theta}^{\rm T}}\left(\frac{\partial\boldsymbol{J}^{\rm T}}{\partial\boldsymbol{J}}\right)_{\boldsymbol{\theta}^{\rm T}}\left(\frac{\partial\boldsymbol{J}}{\partial\boldsymbol{\theta}'}\right)_{\boldsymbol{J}'}
\end{aligned} \tag{B9}$$

The last three derivatives are available from (i) the toy action–angle relations, (ii) the generating function and (iii) perturbation theory. The derivatives in the curly bracket of the line above are available from the toy angle–action coordinates and the generating function. The derivative that multiplies the curly bracket is problematic, however. Specifically

$$\left(\frac{\partial\boldsymbol{\theta}^{\rm T}}{\partial\boldsymbol{\theta}'}\right)_{\boldsymbol{J}'} = \left(\frac{\partial\boldsymbol{\theta}^{\rm T}}{\partial\boldsymbol{J}}\right)_{\boldsymbol{\theta}}\left(\frac{\partial\boldsymbol{J}}{\partial\boldsymbol{\theta}'}\right)_{\boldsymbol{J}'} + \left(\frac{\partial\boldsymbol{\theta}^{\rm T}}{\partial\boldsymbol{\theta}}\right)_{\boldsymbol{J}}\left(\frac{\partial\boldsymbol{\theta}}{\partial\boldsymbol{\theta}'}\right)_{\boldsymbol{J}'} \tag{B10}$$

The second and last derivatives on the right here are provided by perturbation theory, while the first and third derivatives are in principle available from the generating function. However, the first derivative must be obtained by differentiating $\boldsymbol{\theta} = \partial S/\partial\boldsymbol{J}$, which yields

$$0 = \frac{\partial^2 S}{\partial J_k\partial J_j} + \frac{\partial^2 S}{\partial\theta_i^{\rm T}\partial J_j}\left(\frac{\partial\theta_i^{\rm T}}{\partial J_k}\right)_{\boldsymbol{\theta}}. \tag{B11}$$

Unfortunately, we have no way of computing the first of these double derivatives of S. Fortunately, the first term on the right of equation (B10) is of order the perturbation, whereas the second is not. So we neglect the first term.

This paper has been typeset from a TEX/LATEX file prepared by the author.